Shock wave emission and cavitation bubble generation by picosecond and nanosecond optical breakdown in water

A. Vogel[a)] and S. Busch
Medizinisches Laserzentrum Lübeck, Peter-Monnik-Weg 4, D-23562 Lübeck, Germany

U. Parlitz
Drittes Physikalisches Institut, Universität Göttingen, Bürgerstr. 42-44, D-37073 Göttingen, Germany

(Received 18 December 1995; accepted for publication 22 March 1996)

Shock wave emission and cavitation bubble expansion after optical breakdown in water with Nd:YAG laser pulses of 30-ps and 6-ns duration is investigated for energies between 50 μJ and 10 mJ which are often used for intraocular laser surgery. Time-resolved photography is applied to measure the position of the shock front and the bubble wall as a function of time. The photographs are used to determine the shock front and bubble wall velocity as well as the shock wave pressure as a function of time or position. Calculations of the bubble formation and shock wave emission are performed using the Gilmore model of cavitation bubble dynamics and the Kirkwood–Bethe hypothesis. The calculations are based on the laser pulse duration, the size of the plasma, and the maximally expanded cavitation bubble, i.e., on easily measurable parameters. They yield the dynamics of the bubble wall, the pressure evolution inside the bubble, and pressure profiles in the surrounding liquid at fixed times after the start of the laser pulse. The results of the calculations agree well with the experimental data. A large percentage of the laser pulse energy (up to 72%) is transformed into the mechanical energy E_S and E_B of the shock wave and cavitation bubble, whereby the partitioning between E_S and E_B is approximately equal. 65%–85% of E_S is dissipated during the first 10 mm of shock wave propagation. The pressure at the plasma rim ranges from 1300 MPa (50 μJ, 30 ps) to 7150 MPa (10 mJ, 6 ns). The calculated initial shock wave duration has values between 20 and 58 ns, the duration measured 10 mm away from the plasma is between 43 and 148 ns. A formation phase of the shock front occurs after the ns pulses, but not after the ps pulses where the shock front exists already 100 ps after the start of the laser pulse. After shock front formation, the pressure decays approximately proportional to r^{-2}, and at pressure values below 100 MPa proportional to $r^{-1.06}$. The maximum bubble wall velocity ranges from 390 to 2450 m/s. The calculations of bubble and shock wave dynamics can cover a large parameter range and may thus serve as a tool for the optimization of laser parameters in medical laser applications. © *1996 Acoustical Society of America.*

PACS numbers: 43.25.Vt, 43.25.Yw [MAB]

INTRODUCTION

Laser-induced optical breakdown is a nonlinear absorption process leading to plasma formation at locations where the threshold irradiance for breakdown is surpassed.[1] In recent years, plasma-mediated procedures have been used in various fields of laser medicine for photodisruption, ablation, or lithotripsy.[2,3] Plasma formation is accompanied by the generation of shock waves, and, whenever the application site is located in a liquid environment, it is also associated with cavitation. Sometimes these mechanical effects contribute to the intended effect, e.g., in laser lithotripsy[4,5] or in posterior capsulotomy performed by intraocular photodisruption.[6,7] More often, however, they are the source of unwanted collateral effects limiting the local confinement of laser surgery, e.g., in intraocular tissue cutting near sensitive structures of the eye,[8–11] or in pulsed laser angioplasty, where cavitation leads to a strong dilatation of the vessel walls.[12] Whether the mechanical effects are wanted or unwanted, a characterization of the shock wave propagation and cavitation effects is of interest for an optimization of the surgical procedure.

To characterize the shock wave propagation, we investigated the pressure amplitude p_s at the shock front and the profile of the shock wave as a function of the distance r from the emission center. The rise time of the shock front together with the peak pressure define the pressure gradient to which tissue and cells are exposed. The pressure profile determines the energy content of the shock wave, and influences the tissue displacement during shock wave passage which may be correlated to the degree of cellular damage. The pressure decay as a function of propagation distance determines the potential damage range. For spherical shock waves, this decay is governed by the geometric attenuation of the pressure amplitude together with the energy dissipation at the shock front[13] and the increase of the shock wave duration associated with nonlinear sound propagation.[14] Measurement of $p_s(r)$ together with a determination of the shock wave broadening allows an estimation of the energy dissipation into the tissue. Knowledge of the laws governing the decay of the shock wave amplitude furthermore allows one to cal-

[a)]Corresponding author.

culate pressure values near the emission center from results of far-field measurements which are usually much easier to perform than measurements in the vicinity of the laser plasma.

To characterize the cavitation effects, we investigated the expansion velocity and the maximum size reached by the bubble. They determine the maximum tissue displacement that can be caused by the expansion of the laser plasma, and thus define the potential for a structural deformation on a macroscopic scale.

The maximum size of the cavitation bubble can be easily measured by optical or acoustic methods,[8] and the shock wave pressure in the far field can also readily be measured with a piezoelectric hydrophone, provided that the rise time of the hydrophone is fast compared to the shock wave duration.[15] The initial phase of the bubble expansion, and the shock wave propagation near the emission center are, however, difficult to follow, because the shock wave velocity decreases to a value close to sonic speed within a distance of about 200 μm from the emission center[16] which is reached after less than 130 ns. The resolution must therefore be in the range of a few ns and μm, respectively. The shock wave pressure near the plasma cannot be measured well using a hydrophone. The active element of the pressure sensor is usually flat, and not much smaller than 1 mm^2. When the active element is used to detect a spherical shock wave with strong curvature, the measurement results are distorted, because at each time the shock wave hits only a part of the active element. Furthermore, the hydrophone is easily damaged by the strong pressure transient or the subsequent cavitation events. Optical measurement techniques[16–24] avoid these problems, since they provide a very high temporal and spatial resolution while being noninvasive. Doukas *et al.*[19] were able to determine the pressure amplitude p_s at the shock front as a function of propagation distance with 35 μm spatial and about 20 ns temporal resolution using an optical technique. They measured the average shock wave velocity u_s between two laser foci placed 35 μm apart from each other and calculated p_s from u_s. In the present investigation, the shock wave and bubble wall velocities are obtained through ultrafast photography of the shock wave emission and cavitation bubble expansion with increasing time intervals between the laser pulse and the exposure of the photograph. The time resolution of this technique depends on the exposure time of the photograph and on the steps by which the time interval is increased. It was better than 6 ns in all experiments. The spatial resolution is determined by the imaging optics which was 4 μm. An advantage of the photographic method as compared to optical pump-probe techniques[16,18–22] is that it provides two-dimensional information facilitating the location of the plasma center in each experiment. Interferometric techniques[23,24] allow the measurement not just of p_s, but also of the complete pressure profile of the shock wave. These techniques are, however, complicated and possible only at a distance of more than 200 μm from the laser plasma.[24]

Since measurements of the initial phase of the shock wave emission and bubble expansion are very tedious, it would be desirable to have a method to deduce the respective pressure and velocity values from other measurements which are easier to perform. We therefore applied a numerical technique based on the Gilmore model of cavitation bubble dynamics and the Kirkwood–Bethe hypothesis[25,26] by which the initial phase of shock wave emission and bubble expansion can be calculated from the laser pulse duration, the size of the plasma, and the radius of the maximally expanded cavitation bubble. The results of the calculations are compared to the experimental results obtained by time-resolved photography.

The investigations are performed for laser parameters used in intraocular photodisruption. Most clinical photodisruptors deliver Nd:YAG laser pulses with a duration of 6 to 12 ns and a typical pulse energy of 1–10 mJ.[6,7] At 30 ps pulse duration, the radiant energy required for optical breakdown is more than 20 times lower than at 6 ns.[10,18] Therefore, picosecond pulses with energies in the microjoule range have recently been introduced to increase surgical precision, reduce collateral damage, and investigate applications requiring more localized tissue effects than can be achieved with ns-pulses.[27,28] We employed a Nd:YAG laser system delivering pulses with 30 ps or 6 ns pulse duration, and analyzed the events after 50 μJ and 1 mJ pulse energy, and after an energy of 1 and 10 mJ, respectively. The lower energy values at each pulse duration are approximately three times above the breakdown threshold, and the higher values represent the upper limit of the energy range clinically used. The common energy value of 1 mJ allows a direct comparison of the effects at both pulse durations. To provide reproducible experimental conditions, we used distilled water as a model for the intraocular fluids. This is justified by the fact that the threshold for plasma formation as well as the acoustic impedance are similar in distilled water and in ocular fluids.[27,29]

I. EXPERIMENTS

The experimental arrangement is depicted in Fig. 1. We used a Nd:YAG laser system (Continuum YG 671-10) emitting either ns pulses (6 ns) or ps pulses (30 ps) at a wavelength of 1064 nm. The intensity profile of the laser beam was Gaussian (TEM 0/0) for the ps pulses, and nearly Gaussian for the ns pulses, with a weak ring structure modulating the profile. The pulse energy could be varied without changing the beam profile by means of a rotatable half-wave plate between two polarizers.[10] A part of the laser light was frequency doubled to 532 nm.

The laser pulses were focused into a glass cuvette filled with distilled water. The laser beam was expanded to allow a large focusing angle together with a large distance between focus and cuvette walls. To minimize spherical aberrations, Nd:YAG laser achromats were used for the beam collimation and focusing, and an ophthalmic contact lens (Rodenstock RYM) was built into the cuvette wall. The smooth beam profile and minimization of aberrations ensured that no ''hot spots'' occurred in the focal region of the laser beam and only single plasmas were formed. The convergence angle in water was 14° for the ps pulses and 22° for the ns pulses, and the spot diameters ($1/e^2$ radius of intensity in the focal plane measured with a knife edge technique) were 5.8 and 7.6 μm, respectively. The energy threshold for plasma formation

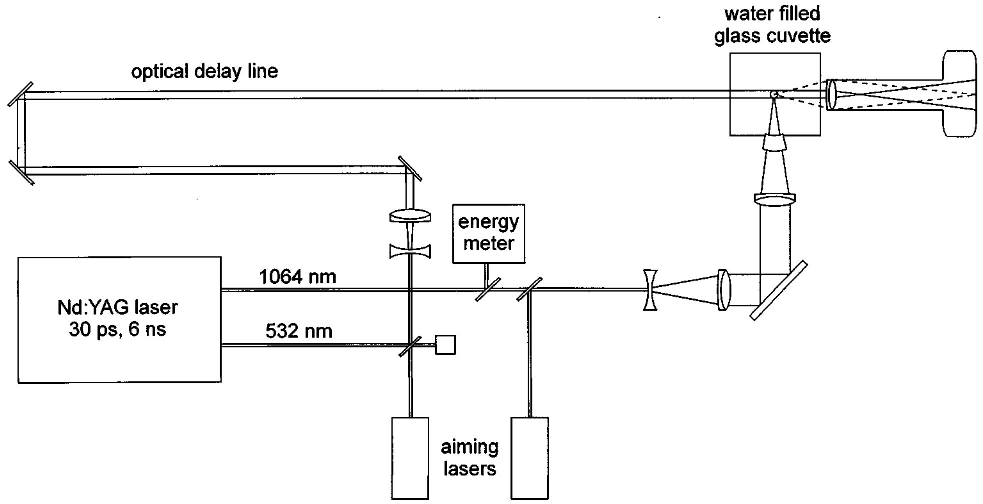

FIG. 1. Experimental arrangement.

(50% breakdown probability) was 7 μJ for the ps pulses and 150 μJ for the ns pulses.

The shock wave emission and cavitation bubble expansion were investigated by taking series of photographs with an increasing time interval between the optical breakdown and the exposure of the photograph.[30] The picture series give values for the propagation velocity of the shock wave which can be used to calculate the corresponding pressure values at the shock front, and they also allow to determine the expansion velocity of the cavitation bubbles. The photographs were taken with 7× magnification on Agfapan APX 25 film using a Leitz Photar lens ($F=3.5$) which provided a spatial resolution of about 4 μm. For the illumination of the photographs we employed the frequency doubled part of the Nd:YAG laser pulses. The illumination pulses were optically delayed by 2–136 ns with respect to the pulses at 1064 nm that were focused into the cuvette.[31] The time delay between laser pulse and photograph was varied in steps of 1 ns up to a delay of 10 ns, in steps of 2 ns up to a delay of 20 ns, and for longer delays in steps of 4 ns. The exposure time of the photographs is given by the duration of the illuminating laser pulse, i.e., it was 30 ps for shock waves induced by ps pulses, and 6 ns in the case of ns pulses.

We investigated the events after ps pulses with 50 μJ and 1 mJ energy, and after ns pulses with 1 and 10 mJ energy. During each laser exposure, the pulse energy was measured using a pyroelectric energy meter (Laser Precision Rj 7100). Before the measurements, the energy meter had been calibrated against a second instrument directly in front of the glass cuvette. To ensure good reproducability between the individual breakdown events, only those photographs were selected, where the pulse energy was within $\pm 7\%$ from the desired value for ps pulses and within $\pm 2\%$ for ns pulses. The shock wave and bubble radius were obtained by measuring the respective diameters at the location of the plasma center and dividing those values by two. For each delay time, the measurement values from six photographs were averaged.

The distances r traveled by the shock wave and the bubble wall were plotted as a function of the delay time t, and curves were fitted through the measurement points using a curve fitting program (Table curve, Jandel Scientific). From the slope of the $r(t)$ curves, the shock wave velocity $u_s(t)$ and bubble wall velocity $u_B(t)$ were derived. From the u_s values, the shock pressure $p_s(r)$ was calculated using the relationship

$$p_s = c_1 \rho_0 u_s (10^{(u_s - c_0)/c_2} - 1) + p_\infty . \tag{1}$$

Here ρ_0 denotes the density of water before compression by the shock wave, c_0 is the normal sound velocity in water, $c_1 = 5190$ m/s, $c_2 = 25\,306$ m/s, and p_∞ is the hydrostatic pressure. The above relationship is based on the conservation of momentum at a shock front[13]

$$p_s - p_\infty = u_s u_p \rho_0 , \tag{2}$$

and on the Hugoniot curve data determined by Rice and Walsh[32]

$$u_p = c_1 (10^{(u_s - c_0)/c_2} - 1), \tag{3}$$

whereby u_p is the particle velocity behind the shock front.

The determination of the shock pressure by measuring the shock wave velocity is accurate only in a small region of less than 1 mm^3 around the emission center, where the difference between shock velocity and sound velocity is well detectable. At a propagation velocity close to the sound velocity, the uncertainty of the velocity determination is approximately 20 m/s, corresponding to an uncertainty of about 15 MPa for the pressure values. In the far field, where the portion of the shock wave intersecting the active area of the pressure transducer can be approximated by a plane wave, hydrophone measurements are thus more accurate, besides being easier to perform. In this range, we used a PVDF hydrophone (Ceram) with a rise time of 12 ns, an active area of 1 mm^2, and a sensitivity of 280 mV/MPa (calibrated by the manufacturer up to a frequency of 10 MHz). The hydrophone was connected to an oscilloscope with 1 MΩ input impedance (open-circuit regime) to ensure proportionality between voltage and pressure.[33]

Parameters required for the numerical calculations of shock wave emission and bubble expansion are the size of the laser plasma and the radius of the maximally expanded cavitation bubble. The plasma size was recorded by open-shutter photography in a darkened room. The bubble radius was determined by measuring the time interval between the two shock waves originating from the optical breakdown and from the bubble collapse. Lauterborn[34] has demonstrated that the expansion and collapse of laser-induced bubbles are highly symmetrical, if the laser pulse duration is much shorter than the oscillation period of the bubble, and if the viscosity of the liquid is small. This is the case for bubble generation in water using laser pulses with durations in the nanosecond or picosecond range. The time interval between the pressure pulses originating from bubble generation and collapse, respectively, is then twice the collapse time T_c, and the bubble radius $R_{\max}$ is given by[35]

$$R_{\max}=T_c/0.915\left(\frac{\rho_0}{p_\infty-p_\nu}\right)^{0.5}, \tag{4}$$

whereby p_ν is the vapor pressure inside the bubble (2330 Pa at 20 °C).

II. NUMERICAL CALCULATIONS

We used the Gilmore model of cavitation bubble dynamics[25,26] to calculate the temporal development of the bubble radius and the pressure inside the bubble, as well as the pressure distribution in the surrounding liquid. The model considers the compressibility of the liquid surrounding the bubble, viscosity and surface tension. It assumes a constant gas content of the bubble, neglecting evaporation, condensation, gas diffusion through the bubble wall, and heat conduction. Heat and mass transfer strongly influence the pressure reached during bubble collapse,[36] but are probably of little importance for the dynamic behavior during the initial stages of the laser-induced bubble expansion. The bubble dynamics is described by the equation

$$\dot{U}=\left[-\frac{3}{2}\left(1-\frac{U}{3C}\right)U^2+\left(1+\frac{U}{C}\right)H + \frac{U}{C}\left(1-\frac{U}{C}\right)R\,\frac{dH}{dR}\right]\cdot\left[R\left(1-\frac{U}{C}\right)\right]^{-1}. \tag{5}$$

Here, R is the radius of the bubble, $U=dR/dt$ is the bubble wall velocity, C is the speed of sound in the liquid at the bubble wall, and H is the enthalpy difference between the liquid at pressure $P(R)$ at the bubble wall and at hydrostatic pressure p_∞:

$$H=\int_{p_\infty}^{P(R)}\frac{dp}{\rho}, \tag{6}$$

whereby ρ and p are the density and pressure within the liquid. Assuming an ideal gas inside the bubble, the pressure P at the bubble wall is given by

$$P=\left(p_\infty+\frac{2\sigma}{R_n}\right)\left(\frac{R_n}{R}\right)^{3\kappa}-\frac{2\sigma}{R}-\frac{4\mu}{R}\,U, \tag{7}$$

whereby σ denotes the surface tension, μ the dynamic shear viscosity, and κ the ratio of the specific heat at constant pressure and volume. The pressure P is assumed to be uniform throughout the volume of the bubble. R_n is the equilibrium radius of the bubble, where the pressure inside the bubble equals the hydrostatic pressure. R_n is thus a measure of the gas content of the bubble. The equation of state of water is approximated by the Tait equation with $B=314$ MPa, and $n=7$:[37]

$$\frac{P+B}{p_\infty+B}=\left(\frac{\rho}{\rho_0}\right)^n, \tag{8}$$

which leads to the following relationships for the Enthalpy H and sound velocity C at the bubble wall:

$$C=(c_0^2+(n-1)H)^{1/2}, \tag{9}$$

$$H=\frac{n(p_\infty+B)}{(n-1)\rho_0}\left[\left(\frac{P+B}{p_\infty+B}\right)^{(n-1)/n}-1\right]. \tag{10}$$

Direct modeling of the temporal evolution and spatial distribution of the energy deposition during optical breakdown[38,39] is complicated, and the details depend strongly on the laser pulse duration.[40] We therefore neglect the details of the breakdown process and refer only to the plasma size at the end of the laser pulse, and to the maximum radius reached by the cavitation bubble as a consequence of plasma expansion. The extent of the plasma marks the volume into which laser energy is deposited, and the size of the expanded cavitation bubble is an indicator for the conversion efficiency of light energy into mechanical energy. The calculations start with a (virtual) bubble nucleus at equilibrium with radius R_0, whereby the volume of this nucleus is identified with the photographically determined plasma size. The energy input during the laser pulse is simulated by raising the value of the equilibrium radius R_n from its small initial value $R_{na}=R_0$ to a much larger final value R_{nb}.[41] Since R_n is a measure of the gas content of the cavitation bubble, an increase of its value implies that the pressure inside the bubble rises and the bubble starts to expand from its initial radius R_0. The R_{nb} value is chosen such that the calculation yields the same maximum cavitation bubble size $R_{\max}$ as determined experimentally. The temporal evolution of the laser power P_L during one pulse is modeled by a $\sin^2$ function with duration τ (full-width at half-maximum), and total duration 2τ:

$$P_L=P_{L0}\,\sin^2\left(\frac{\pi}{2\tau}\,t\right),\quad 0\leqslant t\leqslant 2\tau. \tag{11}$$

It is assumed that the volume increase ΔV_n of the equilibrium bubble at each time t during the laser pulse is proportional to the laser pulse energy E_L:

$$\Delta V_n(t)=(4\pi/3)[R_n^3(t)-R_{na}^3]=kE_L(t) \tag{12}$$

with

$$E_L(t)=\int_0^t P_{L0}\,\sin^2\left(\frac{\pi}{2\tau}\,t\right)dt=P_{L0}\left[\frac{t}{2}-\frac{\tau}{2\pi}\,\sin\left(\frac{\pi}{\tau}\,t\right)\right]. \tag{13}$$

The total energy of the laser pulse is, in analogy to Eqs. (12) and (13), given by

$$E_{L\ \mathrm{tot}}=\frac{\Delta V_{n\ \mathrm{tot}}}{k}=\frac{4\pi}{3k}\,(R_{nb}^3-R_{na}^3) \tag{14}$$

and

$$E_{L\ \mathrm{tot}}=\int_0^{2\tau} P_{L0}\sin^2\left(\frac{\pi}{2\tau}t\right)dt=P_{L0}\tau \tag{15}$$

which leads to $P_{L0}=(4\pi/3k\tau)(R_{nb}^3-R_{na}^3)$. After substituting this expression for P_{L0} into Eq. (13), combination of Eqs. (12) and (13) yields

$$\frac{4\pi}{3}[R_n^3(t)-R_{na}^3]=\frac{4\pi}{3}(R_{nb}^3-R_{na}^3)\times\left[\frac{t}{2}-\frac{\tau}{2\pi}\sin\left(\frac{\pi}{\tau}t\right)\right]. \tag{16}$$

Rewriting leads to the following equation for the temporal development of the equilibrium radius R_n during the laser pulse:

$$R_n(t)=\left\{R_{na}^3+\frac{R_{nb}^3-R_{na}^3}{2\tau}\left[t-\frac{\tau}{\pi}\sin\left(\frac{\pi}{\tau}t\right)\right]\right\}^{1/3}. \tag{17}$$

The differential equation (5) describing the bubble dynamics was integrated numerically with a predictor-corrector method.[42] The constants used for water at a temperature of 20 °C were density of water $\rho_0=998$ kg/m^3, surface tension $\sigma=0.072583$ N/m, polytropic exponent $\kappa=4/3$, coefficient of the dynamic shear viscosity $\mu=0.001046$ Ns/m^3, velocity of sound $c_0=1483$ m/s, and static ambient pressure $p_\infty=100$ kPa.

The solution of Eq. (5) was used to calculate the pressure distribution in the liquid surrounding the cavitation bubble.[25,26] The calculation is based on the Kirkwood–Bethe hypothesis which expresses that the quantity $y=r(h+u^2/2)$ is propagated outward along a path, or a ''characteristic,'' traced by a point moving with the velocity $c+u$, where c is the local velocity of sound in the liquid, u is the local liquid velocity, and h is the enthalpy difference between liquid at pressures p and p_∞. The Kirkwood–Bethe hypothesis leads to the differential equations

$$\dot{u}=-\frac{1}{c-u}\left[(c+u)\frac{y}{r^2}-\frac{2c^2u}{r}\right],\quad \dot{r}=u+c, \tag{18}$$

with

$$c=c_0\left(\frac{p+B}{p_\infty+B}\right)^{(n-1)/2n}. \tag{19}$$

The pressure p at $r=r(t)$ is given by

$$p=(p_\infty+B)\left[\left(\frac{y}{r}-\frac{u^2}{2}\right)\cdot\frac{(n-1)\rho_0}{n(p_\infty+B)}+1\right]^{n/(n-1)}-B. \tag{20}$$

Numerical solution of Eq. (18) with the bubble radius R, the bubble wall velocity U, and the sound velocity C at the bubble wall as initial conditions yields the velocity and pressure distribution in the liquid along one characteristic. Solution of the equation for many initial conditions, i.e., along many characteristics, allows computation of u and p for a network of points (r,t). To determine $p(r)$ at a certain time, one has to collect a set of points with $t=$constant from this network.

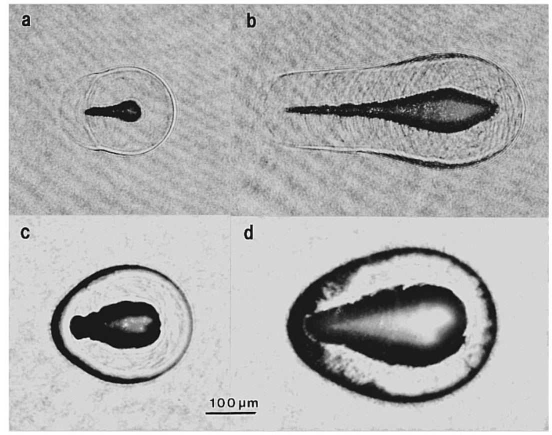

FIG. 2. Plasma, shock wave, and cavitation bubble produced by Nd:YAG laser pulses of different duration and energy: (a) 30 ps, 50 μJ; (b) 30 ps, 1 mJ; (c) 6 ns, 1 mJ; (d) 6 ns, 10 mJ. All pictures were taken 44 ns after the optical breakdown.

III. RESULTS

A. Experiments

Figure 2 presents a comparison of the optical breakdown phenomena occurring with the various laser parameters investigated, and Fig. 3 shows the sequence of events induced by a 1-mJ laser pulse of 30 ps duration, and a 10-mJ pulse of 6 ns duration. The laser light is incident from the right. The location of the beam waist is marked by an arrow (Fig. 3). Shock wave and cavitation bubble appear dark on a bright background, because they deflect the illuminating light out of the aperture of the imaging lens. Although each frame was taken during a different event, the shock wave emission and the initial phase of the bubble expansion can well be followed, because the reproducibility of the events is very good. The arrowheads indicate the locations where the bubble radius and the distance traveled by the shock wave were measured.

The detachment of the shock front from the plasma occurs immediately after plasma formation, because its velocity is always much larger than the particle velocity behind the front.[14] Since the ps plasmas are produced within a time which is short compared to the interframing time, the detachment of the shock front appears to be simultaneous at all plasma sides [Fig. 3(a)]. In contrast to this, the growth of the ns plasmas during the laser pulse can be followed on the picture series shown in Fig. 3(b). The plasma formation begins at the beam waist, and the plasma grows into the cone of the incident laser beam as long as the laser power increases.[38] Correspondingly, the shock wave detachment also starts at the beam waist, and at the side proximal to the laser shock wave detachment is observed only after the end of the plasma growth. At this side, the energy density and the pressure within the plasma is probably higher than at the plasma tip, because here most of the laser light incident during the second half of the pulse will be absorbed. This causes compression waves traveling toward the plasma tip with a velocity $c+u>u_s$.[14] They catch up with the shock front at the end of the picture series, i.e., after about 130 ns. The compression waves behind the shock front lead to a broad-

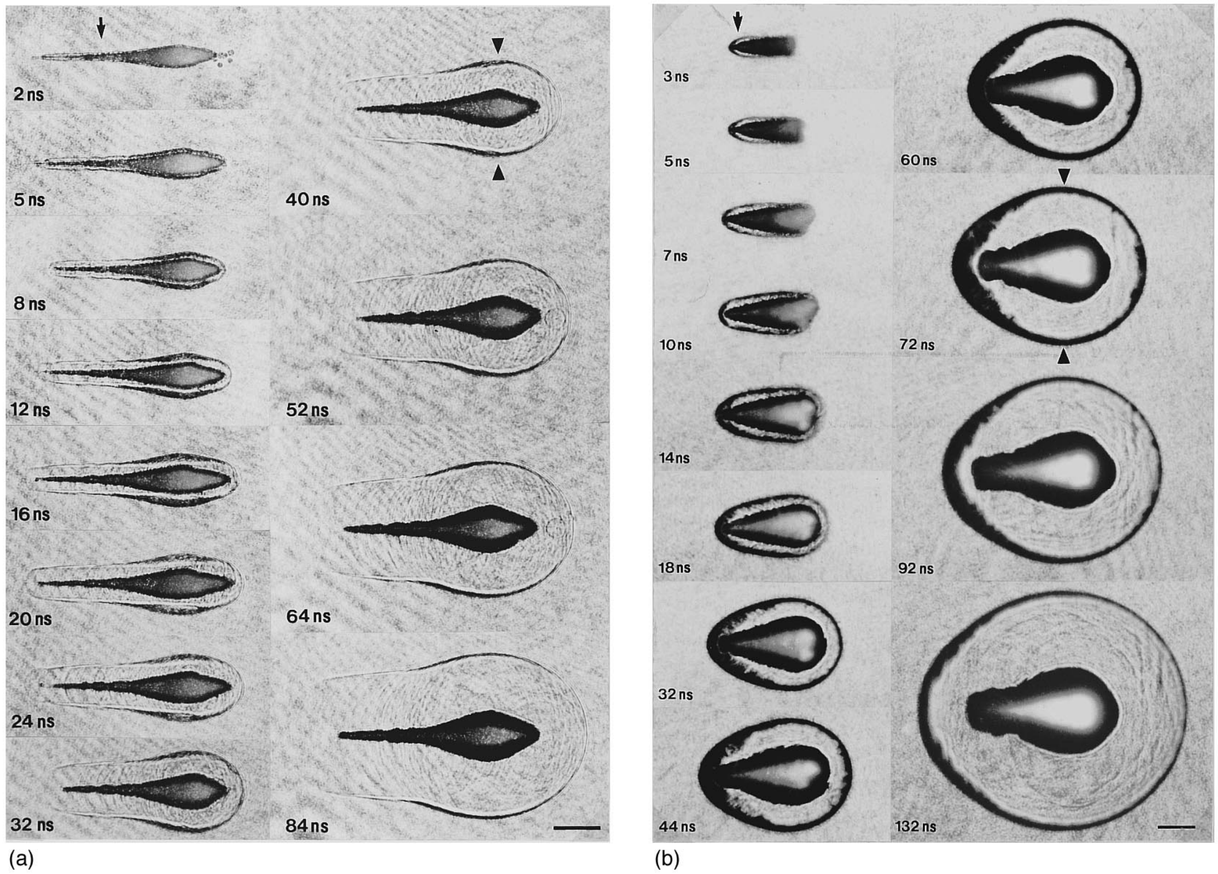

FIG. 3. Shock wave emission and cavitation bubble expansion during the initial phase after optical breakdown caused (a) by a 1-mJ pulse with 30 ps duration, and (b) by a 10-mJ pulse with 6 ns duration. The laser light is incident from the right. The site of the beam waist is marked by an arrow. The time delay of the illumination pulse with respect to the pulse producing the plasma is indicated on each frame. The plasma radiation is visible on each frame, because the photographs were taken in a darkened room with open camera shutter. Shock wave and cavitation bubble, however, are visualized at the time when the illumination pulse passes the object volume. The arrowheads show the location where the bubble radius and the distance traveled by the shock wave were measured. The scales represent a length of 100 μm.

ening of the shock wave image around the plasma tip and thus create the illusion that the shock wave emission is delayed at the side of the beam waist—a statement made by some researchers who did not investigate the time during and immediately after breakdown.[41,43,44]

The quantitative evaluation of the photographic series is shown in Figs. 4–6. In Fig. 4, the distance of the shock front and the bubble wall from the optical axis is plotted as a function of time for the 10-mJ, 6-ns pulse. The $r(t)$ data for the other laser parameters look similar and are not shown. From the curves fitted through the data points we derived the shock wave velocity $u_S(t)$ and the bubble wall velocity $u_B(t)$. They are plotted in Fig. 5 along with the particle velocity $u_p(t)$ behind the shock front. The maximum shock wave velocity is 2500 m/s for the 50-μJ, 30-ps pulse, 2750 m/s for the 1-mJ, 30-ps pulse, 3050 m/s for the 1-mJ, 6-ns pulse, and 4450 m/s (three times the sound velocity in water) for the 10-mJ, 6-ns pulse. These values are slightly higher than the values of 2600 m/s for a 1-mJ ps pulse and 2400 m/s for a 1-mJ ns pulse obtained by Zysset *et al.*[18] with an optical pump-probe technique. The maximum bubble wall velocity is subsonic (390 and 780 m/s) for the ps pulses, and supersonic (1850 and 2450 m/s) for the ns pulses. For all laser parameters, the particle velocity behind the shock front observed during the detachment of the shock wave approximately equals the initial bubble wall velocity. This is due to the fact that shock wave and bubble wall are both driven by the expanding laser plasma. After detachment of the shock front, particle velocity behind the shock front and bubble wall velocity refer to different locations and are therefore no longer directly comparable.

Figure 6 shows the shock wave pressure as a function of the distance r from the optical axis. The maximum pressure value refers to a location at or very close to the plasma rim. It is generally higher for the ns pulses (2400 and 7150 MPa at 1 and 10 mJ) than for ps pulses (1300 and 1700 MPa at 50 μJ and 1 mJ), even at equal energy. The pressure increases with rising pulse energy, whereby this increase is more pronounced with ns pulses. The maximum pressure values observed are about 4–9 times as high as those reported by Doukas *et al.*,[19] because in the present study measurements could be performed closer to the plasma and with better spatial resolution. The slope of the $p_s(r)$ curves in the logarithmic plots is for the ns pulses initially close to -1 and then reaches values larger than -2. For the ps pulses, the slope is steeper than -1 from the very beginning, but stays approximately constant.

Figure 7 presents the results of the far-field measure-

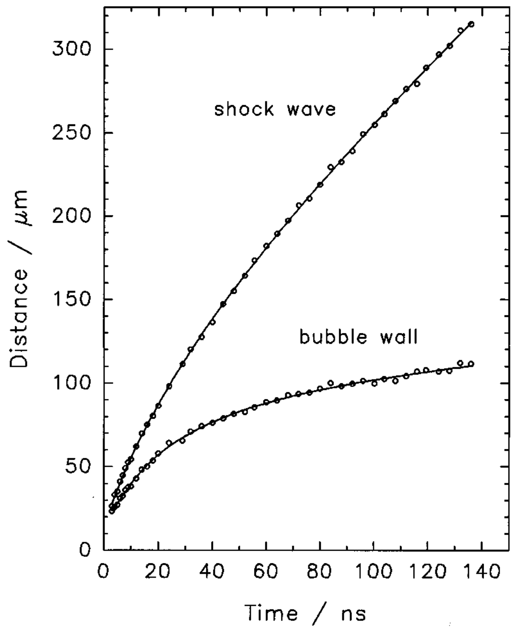

FIG. 4. Propagation of the shock front and the bubble wall perpendicular to the optical axis after a 10-mJ, 6-ns Nd:YAG laser pulse, plotted as a function of the time delay between laser pulse and illumination pulse. Each data point is an average of six measurement values. The standard deviation is $\leqslant 1.0$ μm for time delays up to 30 ns. For longer delays it is $\leqslant 2.4$ μm for the shock wave and $\leqslant 2.8$ μm for the bubble wall. The standard deviation between data points and fit is 1.25 μm for the shock wave position and 1.15 μm for the bubble wall.

ments together with the $p_s(r)$ curves in the near field from Fig. 6. As expected, the pressure decay is slower in the far field than in the near field. The transition between both domains occurs for all laser parameters at a pressure of about 100 MPa. Data points obtained by hydrophone measurements at a distance of less than 5 mm from the emission center of the shock wave are located below the lines fitted to the data at $r \geqslant 5$ mm. This deviation is an artifact due to the detection of a spherical shock wave with a plane PVDF sensor. The stronger the curvature of the shock wave, the smaller is the area of overlap between sensor and shock wave, and the more distorted is the pressure signal. Schoeffmann *et al.*[33] observed a similar phenomenon, but attributed it to cylindrical shock wave emission. This interpretation is certainly not correct in our case, where the plasma is fairly spherical with all laser parameters except the 1-mJ ps pulse (see Fig. 2). Even in the latter case, a nearly spherical form of the shock wave is reached after less than 0.5-mm propagation distance (Fig. 3). It seems therefore reasonable to extrapolate the fit obtained for $r \geqslant 5$ mm to values $r \leqslant 1$ mm as done in Fig. 7. The results obtained by this extrapolation agree very well with the results of the optical measurements performed in the near field of the emission center.

Figure 8 shows shock wave profiles recorded for the various laser parameters at 10 mm distance from the breakdown site. At this distance, the hydrophone measurements are not distorted by geometrical effects. The rise time of the detected pressure signals, however, reflects only the rise time of the hydrophone (12 ns), and the actual rise time of the shock front is below 1 ns.[45–48] The duration of the pressure signals is considerably longer than the response time of the hydrophone and can therefore be considered real. The duration increases with growing pulse energy, and is similar for ns and ps pulses of equal energy (1 mJ).

B. Numerical calculations

Figures 9 and 10 show the calculated bubble wall velocity $U(t)$ and the pressure $P(t)$ inside the bubble during the initial phase of the bubble expansion after laser pulses with 30 ps and 6 ns pulse duration. Figures 11 and 12 present the corresponding pressure distributions $p(r)$ in the liquid surrounding the cavitation bubble at various times t after the start of the laser pulse. For each time t, the position R of the bubble wall and the respective pressure value P at the wall is indicated by a dot. The pressure profiles in the liquid become steeper with time until a shock front is formed. Afterward, the calculations yield ambiguous pressure values, because they do not consider the energy dissipation at the shock front. The ambiguities have no physical meaning, but simply indicate the presence of a discontinuity.[49] The position of the shock front and the peak pressure at the front can be determined using the conservation laws for mass-, impulse-, and energy-flux through the discontinuity. It is defined by a vertical line in the $u(r)$ plots (not shown) cutting off the same area from the ambiguous part of the curve as that added below the curve.[49,50] The location of the front was therefore determined in the $u(r)$ plots and then transferred to the $p(r)$ plots. The reduction of the peak pressure values going along with this procedure represents an overall consideration of dissipation effects at the shock front.

The peak pressure at the bubble wall and the pressure values $p_{\rm peak}$ at the shock front are plotted in Fig. 13 as a function of the distance from the emission center. The shape of the $p_{\rm peak}(r)$ curves agrees qualitatively quite well with the shape of the experimentally determined $p_s(r)$ curves in Fig. 6. The slope of the calculated curves is, however, generally not as steep as that of the measured curves.

IV. DISCUSSION

A. Shock wave emission

1. Equation of state of water

The equation of state (3) determined by Rice and Walsh[32] was used for the experimental investigations, since it is based on relatively recent measurements in a very large pressure range (up to 25 000 MPa). The Gilmore model includes the isentropic Tait equation (8) which fits experimental data for pressure values of up to 2500 MPa.[51] The Tait equation leads to the relationship

$$p_s = (p_\infty + B)\left(\frac{2nu_s^2}{(n+1)c_0^2} - \frac{n-1}{n+1}\right) - B \tag{21}$$

between velocity and pressure at the shock front.[52] In the high pressure domain, Eq. (21) yields lower pressure values for a given shock wave velocity than Eq. (1) based on the Rice and Walsh equation of state. A velocity $u_s = 3000$ m/s, for example, corresponds to a pressure of 2300 MPa accord-

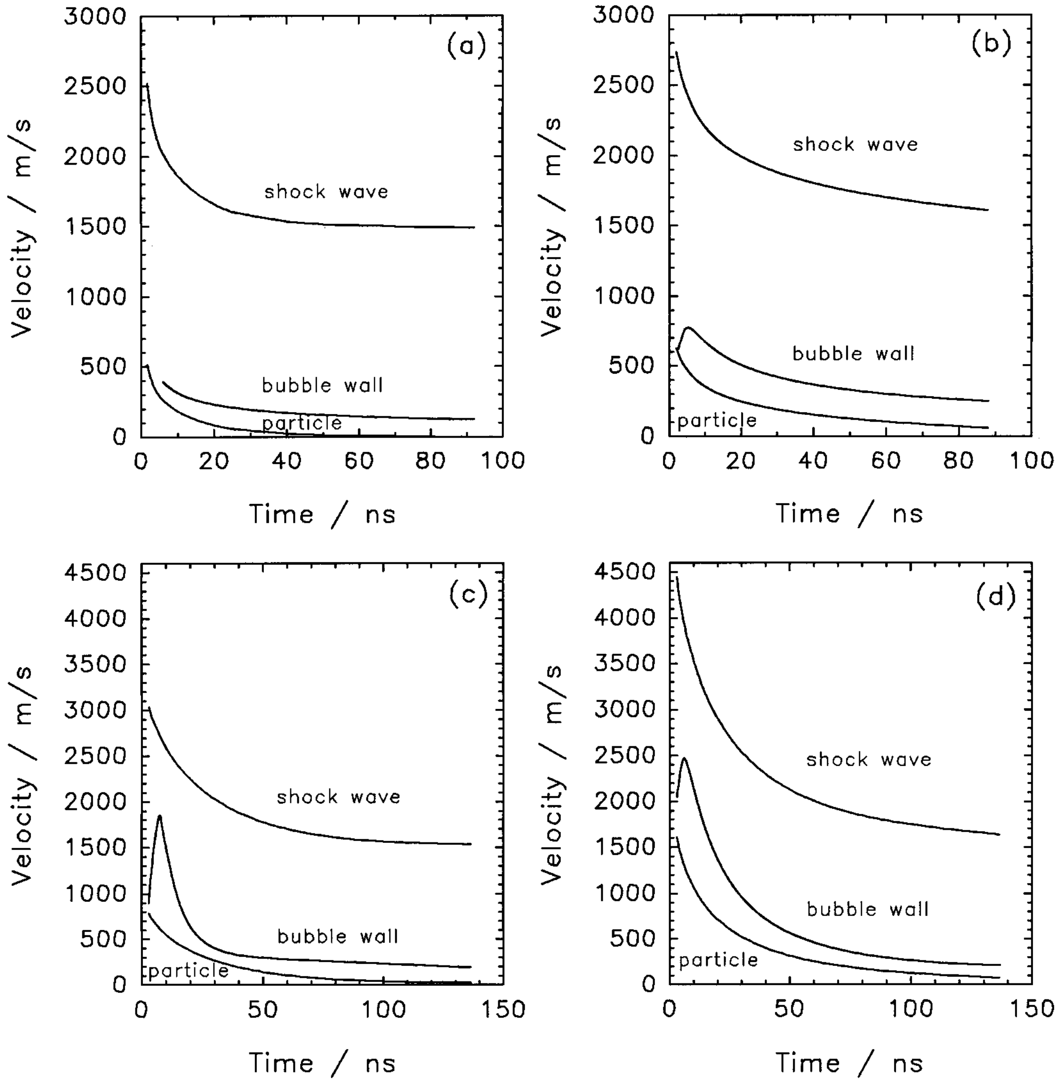

FIG. 5. Experimentally determined shock wave velocity u_s, bubble wall velocity u_B, and particle velocity u_p behind the shock front plotted as a function of the time delay between laser pulse and illumination pulse. The laser parameters are (a) 30 ps, 50 μJ; (b) 30 ps, 1 mJ; (c) 6 ns, 1 mJ; (d) 6 ns, 10 mJ. $u_p(t)$ was calculated from $u_s(t)$ using Eq. (3).

ing to Eq. (1), and to 1620 MPa with Eq. (21). The respective values for $u_s = 4500$ m/s are 7360 and 4515 MPa. The use of two different equations of state hampers the comparison of the experimental and numerical results. Elimination of this drawback would, however, complicate the numerical model, because the Rice and Walsh equation of state cannot easily be incorporated into the Gilmore model.

2. Formation of the shock front

The numerical calculations assume deposition of the laser energy into a bubble nucleus of the size of the laser plasma, with a homogeneous energy distribution inside the nucleus and no energy deposition outside. The pressure rise within the bubble nucleus causes a compression of the surrounding liquid, whereby the leading edge of the compression pulse portrays the temporal shape of the laser pulse. The pressure transients produced by the ps pulses thus have an initial rise time of 30 ps which leads to the formation of a shock front within only 100 ps after the start of the laser pulse (Fig. 11). The pressure transients produced by the ns pulses have a longer initial rise time of about 6 ns, and the evolution of a shock front requires propagation of the pressure pulse for several nanoseconds, corresponding to a distance of about 20 μm (Fig. 12). Shock front formation may take more time than shown in Figs. 11 and 12, if the transition between the high pressure region within the plasma and the surrounding liquid is smoother than assumed in the calculations.

The formation phase of the shock front is also reflected in Figs. 6(b) and 13(b). The slope of the $p_s(r)$ curves in Fig. 6(b) increases gradually with r during a propagation distance of about 60 μm (corresponding to a time of approximately 25 ns). During the formation phase of the shock front, the average slope of the calculated $p_{\mathrm{peak}}(r)$ curve in Fig. 13(a) is -1.02 for the 1-mJ ns pulse, and -1.10 for the 10-mJ pulse, i.e., close to the value of -1 expected in the acoustic approximation. Once the shock front is formed, the slope is much steeper. No change of the slope of the $p_s(r)$ or $p_{\mathrm{peak}}(r)$

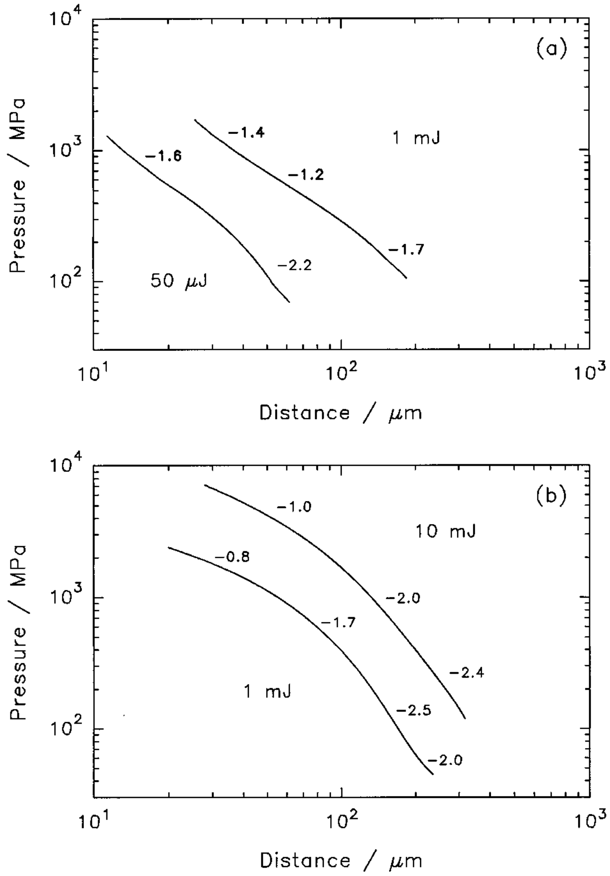

FIG. 6. Experimentally determined shock wave pressure $p_s(r)$ (a) after pulses of 30 ps duration with 50 μJ and 1 mJ energy, and (b) after pulses of 6 ns duration with 1 and 10 mJ energy. The pressure was calculated from the shock wave velocity using Eq. (1). It is plotted as a function of the distance between the shock wave and the optical axis. The numbers indicate the local slope of the $p_s(r)$ curves.

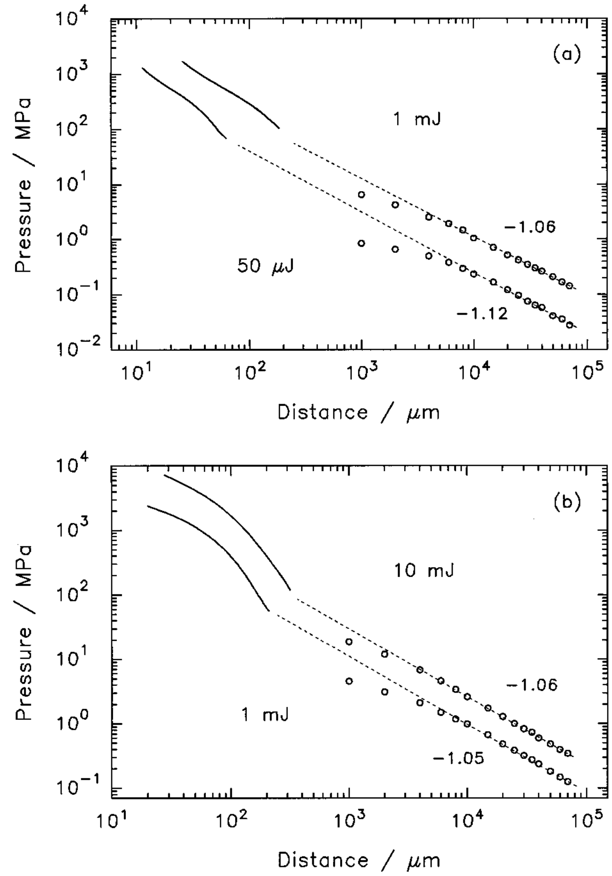

FIG. 7. Logarithmic plot of the decay of the shock wave pressure p_s in the near and far field of the emission center (a) after a 50-μJ and a 1-mJ pulse of 30 ps duration, (b) after a 1- and a 10-mJ pulse of 6 ns duration. The data points represent the results of the far-field hydrophone measurements. The dashed lines are fits to the pressure values measured 5 mm or more away from the emission center. The numbers indicate the slope of the lines.

curves is observed for the ps pulses [Figs. 6(a) and 13(a)], where the shock front exists already after 100 ps.

3. Maximum shock wave pressure

The maximum shock wave pressure is generally higher after ns pulses than after ps pulses, even at equal energy (Table I). Ps-pulses require less radiant energy for optical breakdown and can thus exceed the threshold for plasma formation in a larger volume than ns pulses of the same total energy (see Fig. 2 and Ref. 10). Therefore, the energy density is smaller in ps plasmas and, consequently, also the pressure. For both pulse durations, the peak pressure is higher for the energy value well above the breakdown threshold than for the value close to the threshold. This indicates that the energy density within the plasma grows with increasing pulse energy. The change of energy density is apparently small with ps pulses and larger with ns pulses, but definite conclusions about the pressure dependence of energy require further investigations providing a larger data base.

The calculated maximum bubble pressure almost coincides with the experimentally determined values p_s at the plasma rim for the 1-mJ ps pulse and is only slightly lower than the measured value for the 50-μJ ps pulse. For the 1-mJ ns pulse, however, the calculated value is about twice as high as the experimental value, and it is also higher for the 10-mJ ns pulse. A possible explanation is suggested by the fact that during formation of the shock front produced by a ns pulse the pressure maximum is located *behind* the leading edge of the pressure transient (Fig. 12). It is, however, the leading edge that is detected on the photographs. It propagates slower than the pressure maximum, because the sound velocity is smaller at a lower pressure. Until the shock front has formed completely, the experimentally determined pressure values are therefore lower than the maximum pressure values. This experimental difficulty has consequences also for the $p_s(r)$ curves in Fig. 6(b), since it reduces their initial slope until the shock front has formed completely.

Another source for errors affecting the pressure measurements for ns breakdown is the blur of the shock wave image during the 6 ns of the photographic exposure. The blur can be avoided, when the $r_s(t)$ curve is documented by streak photography with an effective exposure time in the ps range. In this case, maximum pressure values of about 10 000 MPa were obtained after ns pulses of a few millijoule pulse energy.[53]

4. Shock wave width and duration

Table I summarizes the values for the shock wave width and duration immediately after its detachment from the

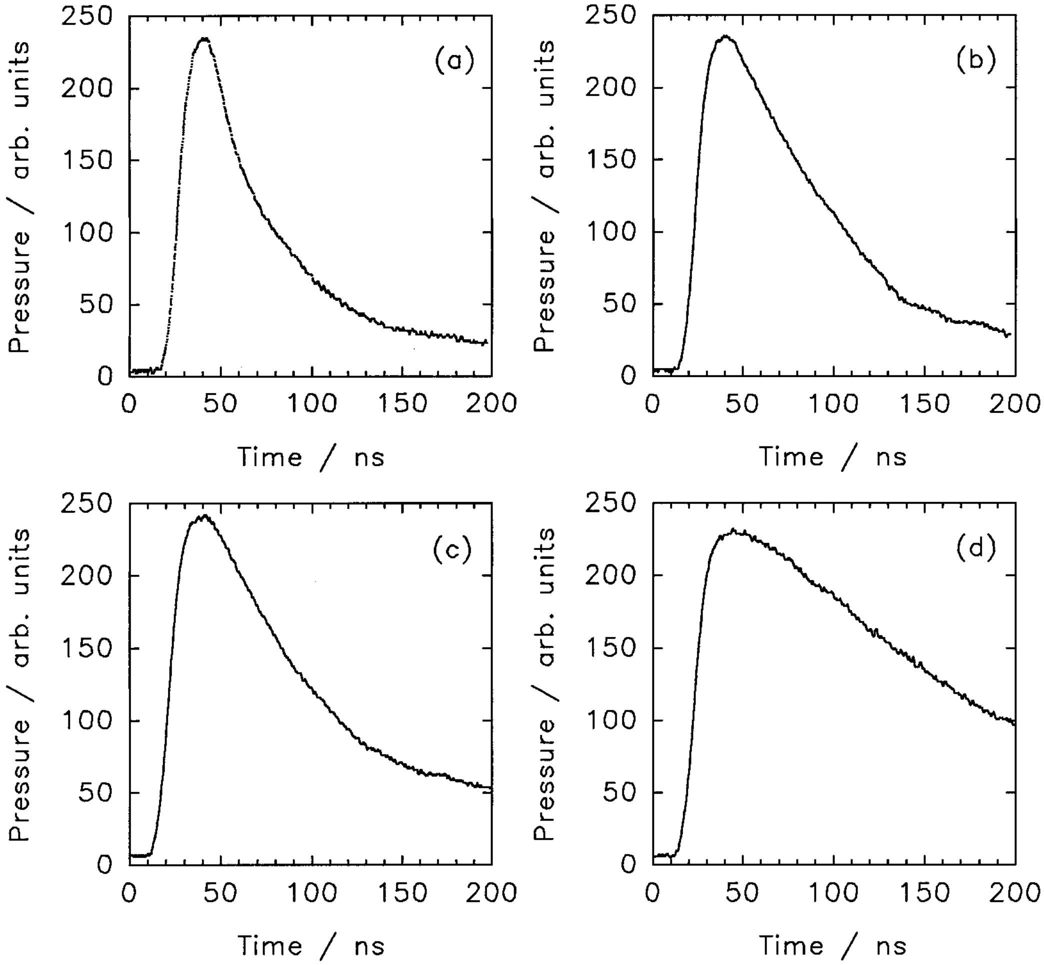

FIG. 8. Hydrophone signals measured at a distance of 10 mm from the emission center of the shock waves. The respective values of laser pulse duration and energy are (a) 30 ps, 50 μJ; (b) 30 ps, 1 mJ; (c) 6 ns, 1 mJ; (d) 6 ns, 10 mJ.

plasma and at 10 mm distance from the emission center. The shock wave width near the plasma (at $r/R_0=6$) was determined from the calculated $p(r)$ profiles in Figs. 11 and 12, and the shock wave duration τ_s was obtained considering the local shock velocity. The duration at 10 mm distance is given by the hydrophone recordings of Fig. 8.

The shock wave duration is longer than the duration of the pressure peak within the cavitation bubble (Figs. 9 and 10), because the pressure at the shock front decreases due to the spherical geometry while the bubble pressure is still relatively high. The shock wave width is broader than the width of the shock wave images on the photographs (Figs. 2 and 3), since the photographs only show the shock front and other parts having a pressure gradient steep enough to deflect the light out of the aperture of the imaging lens. During the detachment process, the gradient behind the shock front is not very steep (Figs. 11 and 12), and therefore this region does not appear dark on the photographs. This suggests that τ_s was underestimated in a previous publication,[10] where it was deduced from the photographs.

The initial shock wave duration is longer for ps pulses than for ns pulses of the same energy. It is, hence, not proportional to the laser pulse duration in the range of pulse durations investigated. The shock wave emission and bubble expansion after ps pulses is an ''impulse response'' to the sudden energy deposition by the laser pulse. The situation is similar at 6 ns pulse duration, because the bubble wall moves very little during the laser pulse. Under these circumstances, τ_s does not depend on the laser pulse duration, but on the initial pressure within the plasma and on the plasma size.[14] The initial pressure is higher in the ns plasmas than in the ps plasmas. Therefore, the cavitation bubble expands faster and the pressure inside the bubble decreases faster, thus shortening the width and duration of the shock wave. This becomes obvious when the shock wave width a_s is normalized with the initial bubble radius R_0 deduced from the plasma size: a_s/R_0 is larger for the ps pulses where it is 3.6–3.8 (see Table I) than for the ns pulses where it amounts to 3.0–3.1. The normalized width is almost independent of the pulse energy, indicating the validity of the similarity principle formulated by Cole (Ref. 14, pp. 110–114). It is interesting to note that the normalized width of laser-induced shock waves closely resembles the value $a_s/R_0=2.5$ calculated by Penney and Dasgupta for the detonation wave produced by a 1800 pound TNT charge (Ref. 14, p. 132), despite of the huge difference in scale. The resemblance is probably due to the similarity of the energy density in TNT (about 5 J/mm^3) and

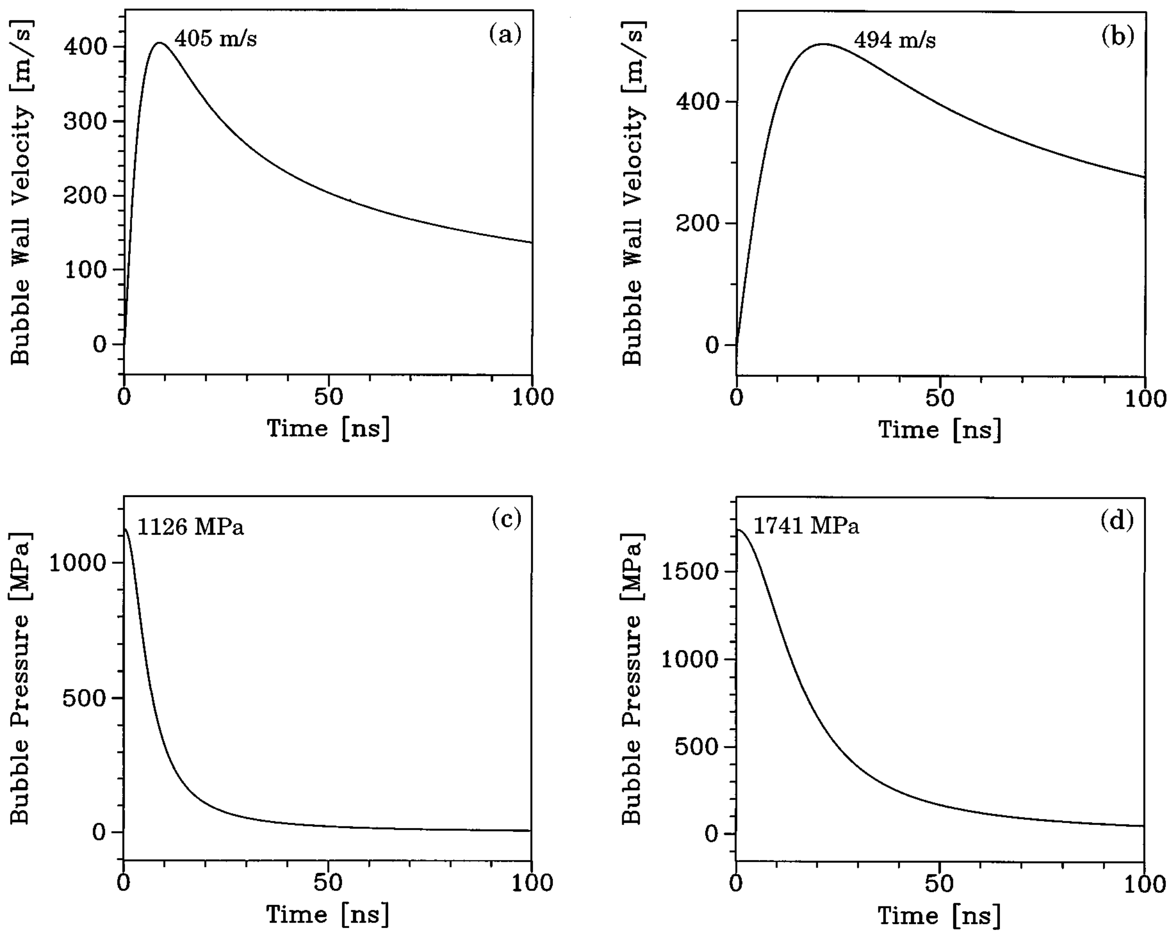

FIG. 9. Results of the numerical calculations for laser pulses with 30-ps duration: Bubble wall velocity $U(t)$ and pressure $P(t)$ inside the bubble during the initial phase of bubble expansion, whereby t denotes the time after the start of the laser pulse. The parameters used were $R_{na}=8.5\ \mu$m, $R_{nb}=87.2\ \mu$m for the 50-μJ pulse (left column), and $R_{na}=26\ \mu$m, $R_{nb}=298.3\ \mu$m for the 1-mJ pulse (right column). R_{na} is the radius of a sphere having the same volume as the laser plasma, and R_{nb} was chosen such that the calculated maximum cavitation bubble size equals the value experimentally obtained (225 μm for the 50-μJ pulse, and 780 μm for the 1-mJ pulse).

in the laser plasma (about 10 J/mm^3 in ps plasmas and 40 J/mm^3 in ns plasmas).

The shock wave duration at a distance of 10 mm from the source is, for all laser parameters, longer than the initial duration close to the plasma because of the nonlinearity of shock wave propagation.[14] The prolongation of shock wave duration is more pronounced for the 1-mJ ns pulse than for the ps pulse at equal energy, probably because of the stronger nonlinearity of sound propagation associated with the higher initial pressure values. The τ_s values at 10 mm vary between 43 ns for the 50 μJ, 30-ps pulse and 148 ns for the 10-mJ, 6-ns pulse. These values agree with the data range reported in Refs. 15, 23, 24, 41, and 54, but are smaller than the values of 200–400 ns reported in Refs. 33 and 55 where higher pulse energies were used.

5. Pressure decay

For spherical acoustic transients, where dissipation and spreading of the pulse width can be neglected, one would expect a pressure decrease proportional to r^{-1}, corresponding to a slope of -1 in the logarithmic plots of the $p_s(r)$ curves in Figs. 6 and 7. The slope is steeper in the case of *shock wave* propagation, where energy is dissipated at the shock front and spreading of the pulse occurs. For the shock waves generated with ns pulses, a slope of more than -2 was measured after shock front formation [Fig. 6(b)]. A proportionality $p_s \propto r^{-2}$ was also determined by Doukas *et al.*[19] for a distance of more than 80 μm from the emission center. The shock wave emission after the 1-mJ ps pulse is almost cylindrical during its initial phase, because the ps plasma has an elongated form. Therefore, the shock wave pressure decays more slowly than after the ns pulse, as indicated by the slope varying between -1.2 and -1.7 in Fig. 6(a). After the 50-μJ pulse, the shock wave is spherical and the decay is faster, with the slope varying between -1.6 and -2.3. For all laser parameters investigated, a transition to a slope of less than -1.2 occurs around a pressure value of about 100 MPa. Similar observations were made by Alloncle *et al.*[56] The decay constant in the far field is between -1.05 and -1.12 (Fig. 7). This agrees well with the work of Schoeffmann *et al.*[33] who reported a value of -1.12 for laser-induced breakdown, and of Arons[57] who found a value of -1.13 for underwater explosions. Arons observed the same decay constant over a range of more than four decades from 0.01 to

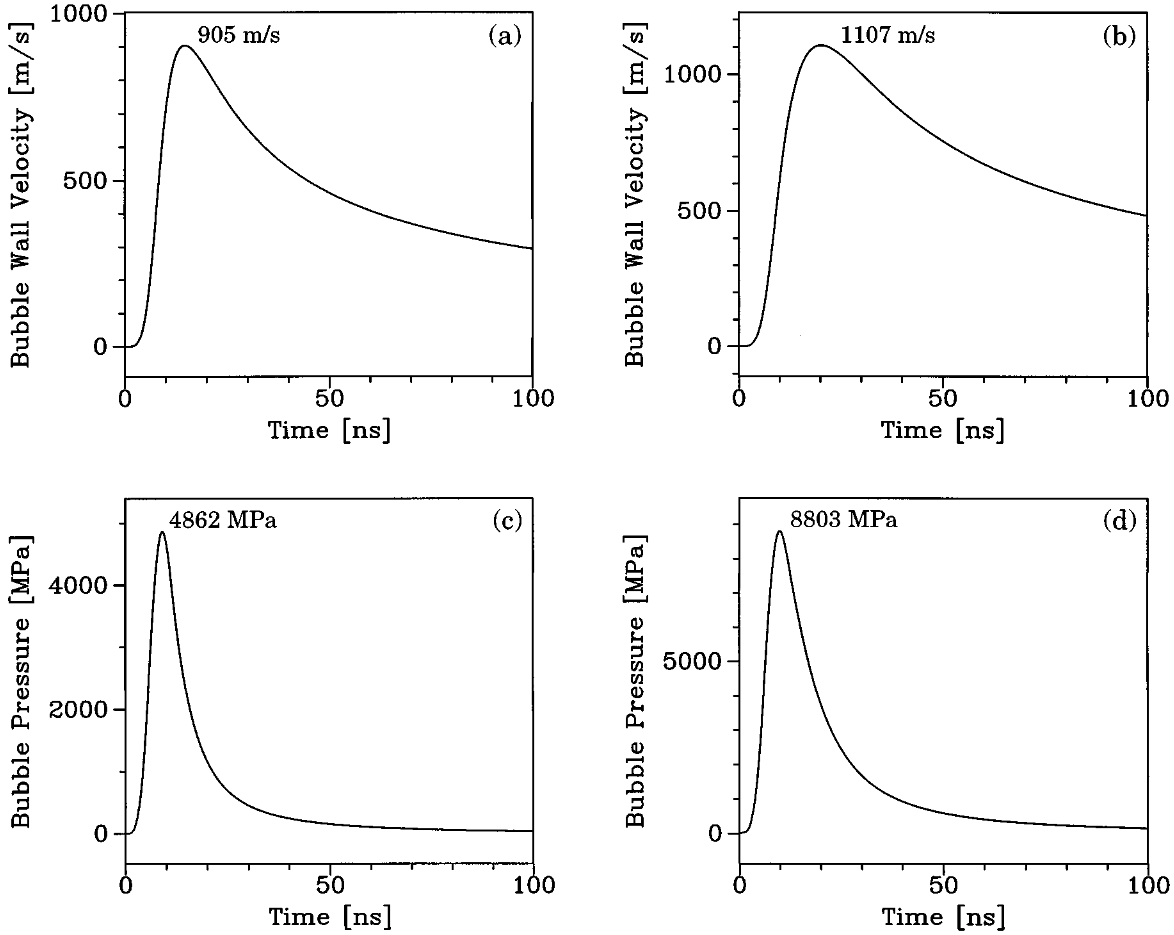

FIG. 10. Results of the numerical calculations for laser pulses with 6 ns duration: Bubble wall velocity $U(t)$ and pressure $P(t)$ inside the bubble during the initial phase of bubble expansion. The parameters used were $R_{na}=18$ μm, $R_{nb}=297$ μm for the 1-mJ pulse (left column), and $R_{na}=37$ μm, $R_{nb}=671$ μm for the 10-mJ pulse (right column). R_{na} corresponds to the measured plasma size, and R_{nb} was chosen such that the calculated maximum cavitation bubble size equals the value experimentally obtained (800 μm for the 1-mJ pulse, and 1820 μm for the 10-mJ pulse).

140 MPa. It should be emphasized that a shock front continues to exist over this whole pressure range once it has formed due to the nonlinearity of sound propagation, even though the shock velocity might asymptotically approach the normal sound velocity.[45,46,58] The ''shock wave range'' of 200–500 μm around a laser plasma reported by some authors[16,18,19] should therefore rather be interpreted as the range, where shock velocity and normal sound velocity are easily distinguishable.

The numerical calculations for ns pulses yield an average slope slightly larger than -1 near the emission center, i.e., in the region where the shock front is still developing [Fig. 13(b)]. The slope of the $p_{\text{peak}}(r)$ curve then increases to a value as large as -1.79 (for the 10-mJ pulse) and decreases again to values of less than -1.4 at a pressure below 100 MPa. A similar shape of the $p_{\text{peak}}(r)$ curve was reported by Akulichev *et al.*[59] for the pressure wave produced during cavitation bubble collapse. In some other theoretical investigations of bubble collapse the calculations were stopped before or just when the shock front appeared,[60,61] and therefore no slope steeper than -1 was observed although the collapse pressure exceeded 2000 MPa.[60]

With ps pulses, the change of the slope is much less pronounced than with ns pulses, since the shock front is formed already 100 ps after the laser pulse. The average slope is smaller than for ns pulses, probably because the normalized shock wave width is broader, providing a relatively larger energy reserve behind the shock front.

The experimental data on shock wave propagation in the pressure range below 100 MPa is well described by the weak-shock solution for underwater explosions.[58,62] The weak shock solution fails, however, to fit the $p_s(r)$ curve at higher pressure values. In this pressure range, the calculations based on Eqs. (18)–(20) are more successful. The overall shape of the calculated $p_{\text{peak}}(r)$ curve looks similar to the experimental $p_s(r)$ curve. The slope of the numerically obtained curve is, however, generally not as steep as that of the experimentally determined curve. An explanation for this discrepancy may be given by the fact that the initial bubble wall velocities obtained with the Gilmore model are below the experimental values (see below). The velocity $c+u$ by which, according to the Kirkwood–Bethe hypothesis, the quantity $r(h+u^2/2)$ propagates into the liquid is therefore too low, and the nonlinearity of sound propagation as well as

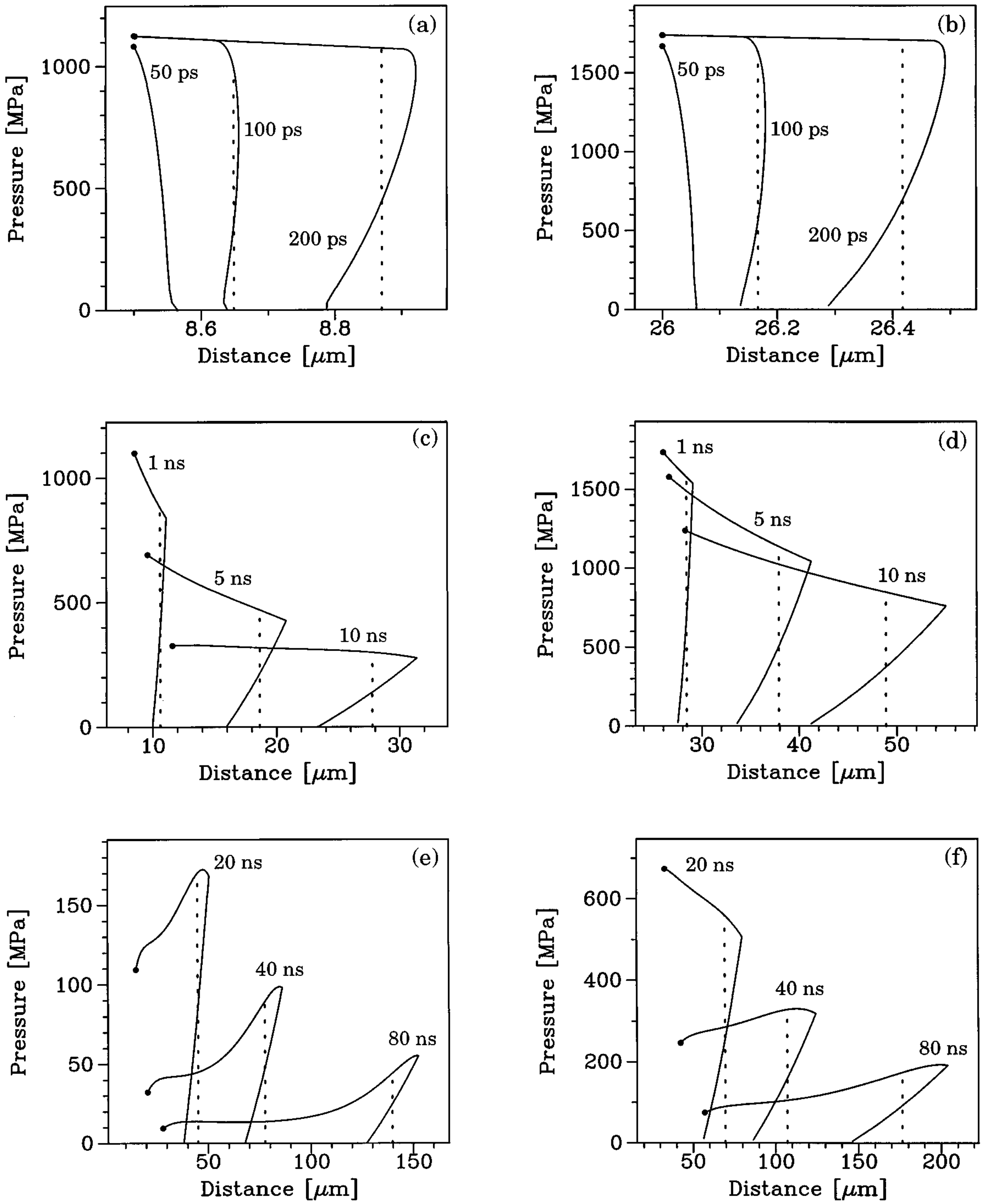

FIG. 11. Calculated pressure distribution in the liquid surrounding the cavitation bubble after a 30-ps laser pulse with 50 μJ pulse energy (left column) and 1 mJ pulse energy (right column). The pressure is plotted as a function of the distance r from the emission center for various times t after the start of the laser pulse. Parameters for the calculations are as in Fig. 9. The dots indicate the pressure P at the bubble wall and the position R of the wall, respectively. For large t values, the location of the shock front is indicated.

the energy dissipation at the shock front are underestimated.

The calculations yield a smooth transition zone between the regime above approximately 100 MPa exhibiting strong damping of the shock wave, and the regime below 100 MPa where only moderate damping occurs. The transition is much more abrupt in the experimental curves for ns pulses in Fig. 7. The discontinuity is most likely not real, but a consequence of the measurement uncertainty of about 15 MPa in this pressure range.

6. Shock wave energy

The shock wave energy is given by[14]

$$E_s = \frac{4\pi R_m^2}{\rho_0 c_0} \int p_s^2 \, dt, \tag{22}$$

whereby R_m denotes the distance from the emission center,

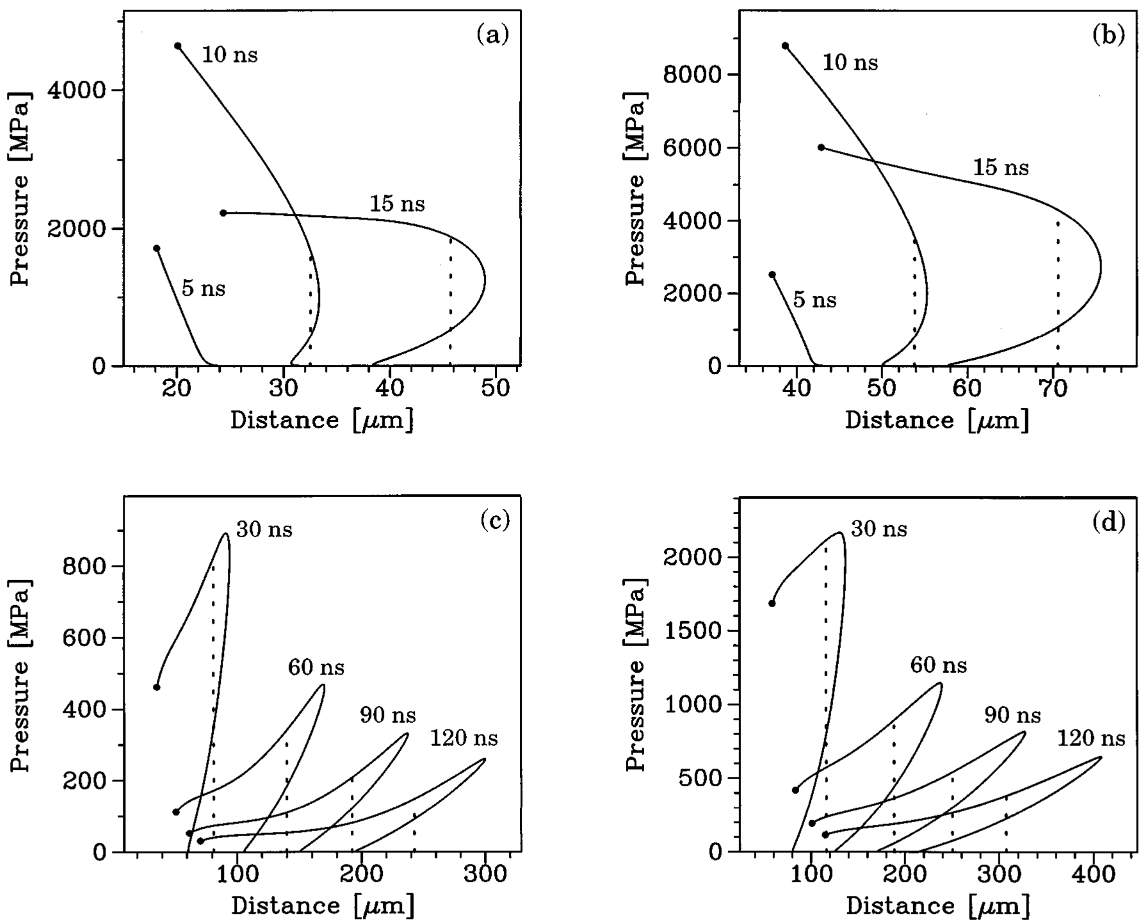

FIG. 12. Calculated pressure distribution in the liquid surrounding the cavitation bubble after a 6-ns laser pulse with 1 mJ pulse energy (left column) and 10 mJ pulse energy (right column). The pressure is plotted as a function of the distance r from the emission center for various times t after the start of the laser pulse. Parameters for the calculations are as in Fig. 10. The dots indicate the pressure P at the bubble wall and the position R of the wall, respectively. For large t values, the location of the shock front is indicated.

where the pressure p_s is measured. Assuming an exponential shock wave profile,[14] and identifying R_m with the center of the profile, we calculated the shock wave energy at the normalized distance $r/R_0=6$ and at a distance $r=10$ mm (Table I). The calculation for the near field is based on the numerically determined shock wave profiles, and the energy in the far field is obtained from the hydrophone signals in Fig. 8. The E_s value at $r/R_0=6$ for the 1-mJ ps pulse may be slightly overestimated, because at this distance the shock wave is not yet spherical as presumed in Eq. (22).

The conversion of light energy into acoustic energy ranges from 8.9% for the 50-μJ, 30-ps pulse to 41.9% for the 10-mJ, 6-ns pulse. The conversion efficiency is higher for ns pulses, because they produce more compact plasmas with a higher energy density, and it is higher for the pulse energies well above the optical breakdown threshold, because a larger energy fraction is absorbed in the plasma. During propagation of the first 10 mm, 65%–85% of the acoustic energy is dissipated into the liquid. The damping is higher for the ns pulses, because they create a higher initial shock wave pressure. Our results show that the conversion of light energy into acoustic energy is largely underestimated, if the acoustic energy is determined from far-field measurements as done in an earlier study.[15]

B. Cavitation bubble expansion

1. Bubble wall velocity

The maximum measured bubble wall velocity is subsonic for the ps pulses and supersonic for the ns pulses (Table II). The initial bubble wall velocity approximately equals the initial particle velocity behind the shock front (Fig. 5). This agrees with theoretical considerations that $u_B=u_p$ at $t=0$, if the energy is deposited instantaneously.[63] Afterward, the measured bubble wall velocity rises for a few nanoseconds [except in Fig. 5(a), where u_B data are available only at $t\geqslant 6$ ns], and then starts to decrease. These observations lead to the following picture of the early phase of cavitation bubble expansion. Once a plasma with a high pressure inside has been created, the surrounding liquid is compressed and starts to flow radially outward. The compression wave propagates through the liquid and incorporates more and more liquid mass into the radial flow. This flow always starts with a rapid acceleration of the liquid to the particle velocity corresponding to the pressure at the front of the compression wave. The acceleration continues after the shock wave has passed, because the pressure within the expanding cavitation bubble is still high. The radial flow at the bubble wall thus reaches a larger velocity than the initial particle velocity be-

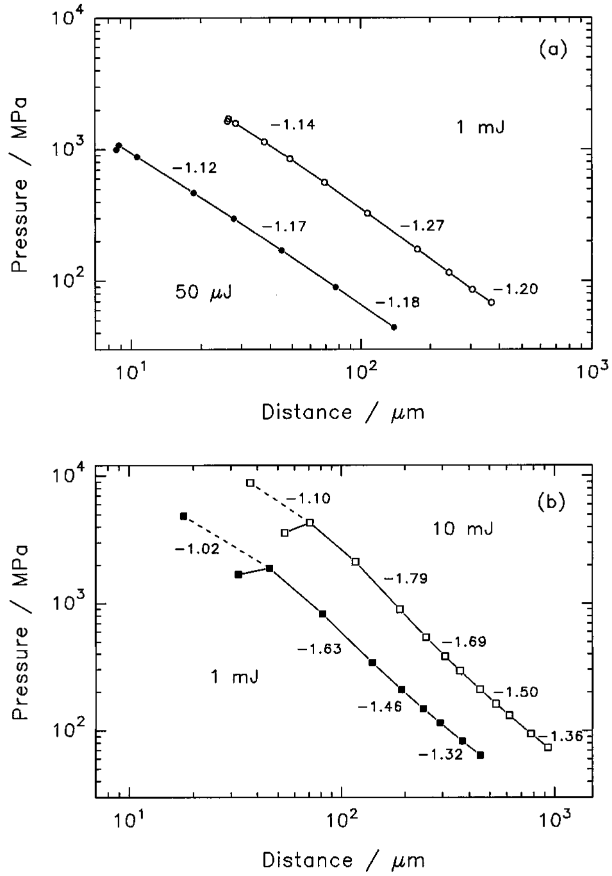

FIG. 13. Numerically determined shock front pressure p_{peak} plotted as a function of the distance r from the emission center (a) after a 30-ps laser pulse with 50 μJ and 1 mJ pulse energy, (b) after a 6-ns laser pulse with 1 and 10 mJ pulse energy. The data points are connected by solid lines to simplify identification of the sets belonging to different laser parameters. For ns pulses, the peak pressure at the bubble wall is also indicated and connected by a dashed line to the peak pressure reached after shock front formation. The numbers indicate the local slope of the $p_{\mathrm{peak}}(r)$ curves.

hind the shock front. With increasing bubble radius, however, the kinetic energy imparted to the liquid is distributed among an ever larger liquid mass. Therefore, the bubble wall velocity starts to decrease again after about 10 ns, although the bubble pressure is still higher than the hydrostatic pressure and continues to drive the bubble expansion.

The calculations yield a slightly different picture (Figs. 9, 10). They show a continuous acceleration of the bubble wall for 10–20 ns during which the bubble wall velocity is smaller than the particle velocity behind the shock front given by Eq. (3). We believe that this inconsistency is a shortcoming of the Gilmore model, because the jump conditions at a shock front[13] are not all included. The inconsistency becomes especially clear in the case of the 1-mJ ps pulse where, according to Eq. (3), a particle velocity of 630 m/s is reached at the plasma rim (or bubble wall, respectively) after only 30 ps. The calculated maximum of the bubble wall velocity, however, is below 500 m/s and reached only after 20 ns. For all other laser parameters, the calculated maximum bubble wall velocity is also lower and reached later than the maximum observed experimentally. The discrepancy grows with increasing pulse energy. At 100 ns after the laser pulse, the calculated velocity values are, on the other hand, higher than the measured values (see Figs. 9 and 10 in comparison to Fig. 5). This way, the kinetic energy of the radial fluid flow grows large enough for the bubble to reach the same size as experimentally observed.

TABLE I. Summary of experimental and numerical results for the shock wave emission.

	30 ps, 50 μJ	30 ps, 1 mJ	6 ns, 1 mJ	6 ns, 10 mJ
Measured pressure p_s at plasma rim [MPa]	1300	1700	2400	7150
Calculated max. bubble pressure P [MPa]	1126	1741	4861	8801
Calculated shock wave width a_s [μm] at $r/R_0=6$	32	93	54	114
Calculated shock wave duration τ_s [ns] at $r/R_0=6$	20	53	33	58
a_s/R_0 at $r/R_0=6$	3.8	3.6	3.0	3.1
Calculated shock wave energy E_S [μJ] at $r/R_0=6$	4.44	214	309	4190
Conversion of light energy E_L into shock wave energy E_S [%]	8.9	21.4	30.9	41.9
Measured shock wave pressure p_s [MPa] at $r=10$ mm	0.24	1.06	0.99	2.62
Measured shock wave duration τ_s [ns] at $r=10$ mm	43	70	77	148
Shock wave energy E_s [μJ] at $r=10$ mm	1.52	48	46.2	622
Dissipation of shock wave energy within 10 mm [%]	65.8	77.5	85.0	85.2

2. Bubble energy

The bubble energy is given by

$$E_B=(4/3)\pi R_{\max}^3(p_0-p_\nu) \tag{23}$$

and its values for the different laser parameters are listed in Table II. For ps pulses, E_B is about the same as the shock wave energy E_S near the plasma, and for ns pulses it amounts to about two thirds of the shock wave energy. E_B is, however, always 3–4 times larger than the acoustic energy determined 10 mm away from the plasma.

TABLE II. Summary of experimental and numerical results for the bubble expansion.

	30 ps, 50 μJ	30 ps, 1 mJ	6 ns, 1 mJ	6 ns, 10 mJ
Measured max. bubble wall velocity u_B [m/s]	390	780	1850	2450
Calculated max. bubble wall velocity U [m/s]	405	494	905	1106
Max. bubble radius $R_{\max}$ [μm]	225	780	800	1820
Bubble energy E_B [μJ]	4.7	197	212	2500
Conversion of light energy E_L into bubble energy E_B [%]	9.4	19.7	21.2	25.0

TABLE III. Conversion of light energy into mechanical energy and evaporation energy.

	30 ps, 50 μJ	30 ps, 1 mJ	6 ns, 1 mJ	6 ns, 10 mJ
Conversion of light energy E_L into mechanical energy (E_S+E_B) [%]	18.2	42.5	50.6	72.4
Conversion of light energy E_L into evaporation energy E_v [%]	13.4	19.2	6.3	5.5
$E_v/(E_S+E_B)$	0.74	0.45	0.12	0.08

C. Tissue effects of cavitation bubble and shock wave

The fraction $(E_S+E_B)/E_L$ of the laser pulse energy converted into mechanical energy ranges from 18.2% for the 50-μJ ps pulse to 72.4% for the 10-mJ ns pulse (Table III). These percentages refer to the light energy incident on the contact lens in the glass cuvette (Fig. 1). A complete energy balance is beyond the scope of this paper, but it is of interest for intraocular microsurgery to compare the mechanical energy (E_S+E_B) with the energy E_v required for evaporation of the liquid within the plasma volume. The latter part is essential for the cutting of tissue, whereas the mechanical effects accompanying plasma formation are the main cause of tissue disruption and collateral damage.[9] The ratio $E_v/(E_S+E_B)$ is 6–7 times higher for ps pulses than for ns pulses both near the breakdown threshold and well above threshold (Table III). Ps pulses are thus better suited for tissue cutting with little disruptive side effects.

Cavitation bubble and shock wave take away similar fractions of the laser light energy, but act on very different time scales and have different tissue effects. These effects are discussed in the following using the example of a 1-mJ ns pulse and assuming that the acoustic properties of tissue are similar to water. After plasma formation, the tissue is first exposed to the passage of the shock wave lasting 30–80 ns, depending on the distance from the plasma. The shock front has a rise time of only 20 ps when the pressure jump is 600 MPa,[48] and a rise time of about 700 ps when the pressure jump is 10 MPa.[46] According to our results, the shock front is formed when the pressure pulse has travelled a distance of approximately 50–60 μm from the emission center. The peak pressure is then about 1000 MPa. A pressure jump of this amplitude is associated with a compression of the tissue by a factor of 1.22—occurring within about 20 ps. The fast compression leads to a transformation of kinetic energy into heat resulting in a temperature rise of 30 °C.[13] Most of the shock wave energy are probably dissipated in the strong shock wave regime at a pressure above 100 MPa, i.e., within the first 200 μm of its propagation. The interaction between shock front and tissue is at each time confined to a very small region in the nm range. The particle displacement during shock wave passage is also fairly small, in spite of the high particle velocity behind the shock front. It is approximately given by $d=\tau_s u_p$ and amounts to 14 μm immediately after the shock front has formed. At a distance of 0.8 mm, which is the maximal cavitation bubble radius, it is only 0.5 μm. Local variations of the sound velocity within the tissue may lead to a distortion of the shock front resulting in shearing forces, but these distortions are leveled out fast, because compression waves behind the shock front traveling at a velocity $c+u>u_s$ feed energy preferentially into those parts of the shock front lagging behind. We can conclude that all shock wave-induced tissue effects are confined to very small dimensions on a cellular or subcellular level.

The situation is quite different for the cavitation bubble expansion. The maximum bubble wall velocity after the 1-mJ pulse is 1850 m/s and stays above 200 m/s during the first 100 ns. Within this time, the bubble radius increases from 18 to 60 μm. After 73 μs, the maximum bubble radius of 800 μm is reached. The bubble expansion thus leads to a relatively large and initially very fast displacement of the material surrounding the site of plasma formation which can result in tissue alterations on a macroscopic level. The microscopic changes caused by the shock wave weaken the tissue structure in the vicinity of the laser plasma and thus facilitate the occurrence of macroscopic changes during the bubble oscillation. In clinical practice, the cavitation bubble dynamics is often not spherical, and thus bubble migration and jet formation may occur during the collapse phase. This results in an energy concentration away from the application site and may further add to the damage potential of the bubble dynamics.[9]

The minimal pressure of laser-induced shock waves resulting in functional cell damage is approximately 50–100 MPa.[64] After a 1-mJ ns pulse, a pressure of 50 MPa is reached up to a distance of about 250 μm, i.e., in a range of less than one third of the cavitation bubble radius. The mechanical tissue effects in plasma-mediated processes are, hence, dominated by cavitation. The potential range of the shock wave action can, however, reach beyond the maximum bubble radius, if processes focusing the shock wave energy occur. When, for example, the shock wave hits a gas bubble (which may have been produced by earlier laser pulses), the bubble is collapsed and a liquid jet propagating in the direction of the shock wave is formed.[9] This jet can induce tissue damage at a distance of more than four times the maximum cavitation bubble radius.[9]

V. CONCLUSIONS

Shock wave emission and cavitation bubble expansion after optical breakdown with ns and ps pulses were investigated by time-resolved photography and hydrophone measurements, as well as by numerical calculations. The calculations were based on experimentally determined values of the laser pulse duration, plasma size, and maximum cavitation bubble radius, i.e., on easily measurable parameters. The numerical results for the maximum shock wave pressure and the maximum bubble wall velocity agree within a factor of 2 or better with the measured values. This agreement is good, considering the simplifying assumptions made for the calculations and the difficulty to perform measurements with the high temporal and spatial resolution required.

The results of the experiments and calculations complement each other. They yield the following picture of the events after ps and ns optical breakdown:

(1) A large percentage of the laser pulse energy (42.5% for a 1-mJ, 30-ps pulse, and 72% for a 10-mJ, 6-ns pulse) is transformed into the mechanical energy E_S and E_B of shock wave and cavitation bubble. The conversion efficiency is lower for ps pulses than for ns pulses, because with ps pulses a larger percentage of the energy is needed to evaporate the liquid within the plasma volume. Ps pulses are therefore well suited for tissue cutting with little mechanical side effects.

(2) E_S and E_B have similar values after ps breakdown, but after ns breakdown, where the energy density in the plasma is higher, E_S is about 50% larger than E_B. A fraction of 65%–85% of the shock wave energy is dissipated during the first 10 mm of shock wave propagation.

(3) The calculated shock wave duration close to the plasma (at $r/R_0=6$) ranges from 20 to 58 ns, the measured duration at $r=10$ mm from 43 to 148 ns. The prolongation of τ_s with increasing distance is due to nonlinear propagation effects. In the parameter range investigated, τ_s is not correlated to the laser pulse duration, but rather to the plasma size and to the energy density within the plasma. For each pulse duration, the ratio of shock wave width and plasma radius is approximately constant regardless of the pulse energy, i.e., the similarity principle holds.

(4) The measured pressure at the plasma rim ranges from 1300 MPa (50 μJ, 30 ps) to 7150 MPa (10 mJ, 6 ns). The $p_s(r)$ curve for ns pulses shows an initial part with little energy dissipation representing the formation phase of the shock front, a middle part with strong dissipation, and, below approximately 100 MPa, another part with little dissipation (weak shock wave regime). With ps pulses, the shock front is already formed within 100 ps after the start of the laser pulse, and the $p_s(r)$ curve shows dissipation from the very beginning.

(5) The initial bubble wall velocity equals the initial particle velocity behind the shock front when the front detaches from the laser plasma. The maximal bubble wall velocity ranges from 390 m/s (50 μJ, 30 ps) to 2450 m/s (10 mJ, 6 ns).

(6) Shock wave-induced tissue effects occur mainly on a cellular and subcellular level, whereas cavitation results in macroscopic tissue disruption. The mechanical effects observed in plasma-mediated laser surgery are dominated by cavitation.

The numerical model presented in this paper may serve as a tool for the optimization of laser parameters in medical laser applications, since it can easily cover a wide parameter range. The model is not restricted to plasma-mediated effects, but can, in a similar form, also be applied to ablation processes relying on explosive evaporation. In Ref. 65 it was used to identify a strategy for the minimization of cavitation effects during pulsed laser ablation in a liquid environment.

ACKNOWLEDGMENTS

The authors thank Dr. A. Doukas and Joachim Noack, MSc, for fruitful discussions. The investigations were supported by the Deutsche Forschungsgemeinschaft, Grant No. Bi-321/2-3.

[1] Y. R. Shen, *The Principles of Nonlinear Optics* (Wiley, New York, 1984), pp. 528–539.

[2] S. J. Gitomer and R. D. Jones, ''Laser-produced plasmas in medicine,'' IEEE Trans. Plasma Sci. **19**, 1209–1219 (1991).

[3] A. Vogel, ''Nonlinear absorption: Intraocular microsurgery, and laser lithotripsy,'' Phys. Med. Biol. **41** (in press).

[4] P. Teng, N. S. Nishioka, R. R. Anderson, and T. F. Deutsch, ''Acoustic studies of the role of immersion in plasma-mediated laser ablation,'' IEEE J. Quant. Electron. **QE-23**, 1845–1852 (1987).

[5] K. Rink, G. Delacrétaz, and R. P. Salathé, ''Fragmentation process induced by microsecond laser pulses during lithotripsy,'' Appl. Phys. Lett. **61**, 258–260 (1992).

[6] R. F. Steinert and C. A. Puliafito, *The Nd:YAG Laser in Ophthalmology* (Saunders, Philadelphia, 1985).

[7] F. Fankhauser and S. Kwasniewska, ''Neodymium:yttrium-aluminium-garnet laser,'' in *Ophthalmic Lasers*, edited by F. A. L'Esperance (Mosby, St. Louis, MO, 1989), 3rd ed., pp. 781–886.

[8] A. Vogel, W. Hentschel, J. Holzfuss, and W. Lauterborn, ''Cavitation bubble dynamics and acoustic transient generation in ocular surgery with pulsed neodymium: YAG lasers,'' Ophthalmology **93**, 1259–1269 (1986).

[9] A. Vogel, P. Schweiger, A. Frieser, M. N. Asiyo, and R. Birngruber, ''Intraocular Nd:YAG laser surgery: light-tissue interaction, damage range, and reduction of collateral effects,'' IEEE J. Quantum Electron. **QE-26**, 2240–2260 (1990).

[10] A. Vogel, S. Busch, K. Jungnickel, and R. Birngruber, ''Mechanisms of intraocular photodisruption with picosecond and nanosecond laser pulses,'' Lasers Surg. Med. **15**, 32–43 (1994).

[11] J. Mellerio, M. Capon, and F. Docchio, ''Nd:YAG lasers: a potential hazard from cavitation bubble behaviour in anterior chamber procedures?,'' Lasers Ophthalmol. **1**, 185–190 (1987).

[12] T. G. van Leeuwen, J. H. Meertens, E. Velema, M. J. Post, and C. Borst, ''Intraluminal vapor bubble induced by excimer laser pulse causes microsecond arterial dilatation and invagination leading to extensive wall damage in the rabbit.'' Circulation **87**, 1258–1263 (1993).

[13] G. E. Duvall and G. R. Fowles, ''Shock waves,'' in *High Pressure Physics and Chemistry*, edited by R. S. Bradley (Academic, New York, 1963), pp. 209–291.

[14] R. H. Cole, *Underwater Explosions* (Princeton U.P., Princeton, NJ, 1948).

[15] A. Vogel and W. Lauterborn, ''Acoustic transient generation by laser-produced cavitation bubbles near solid boundaries,'' J. Acoust. Soc. Am. **84**, 719–731 (1988).

[16] J. G. Fujimoto, W. Z. Lin, E. P. Ippen, C. A. Puliafito, and R. F. Steinert, ''Time-resolved studies of Nd:YAG laser-induced breakdown,'' Invest. Ophthalmol. Vis. Sci. **26**, 1771–1777 (1985).

[17] K. Hinsch and E. Brinkmeyer, ''Investigation of very short cavitation shock waves by coherent optical methods,'' Proc. SPIE **97**, 166–171 (1976).

[18] B. Zysset, G. Fujimoto, and T. F. Deutsch, ''Time-resolved measurements of picosecond optical breakdown,'' Appl. Phys. B **48**, 139–147 (1989).

[19] A. G. Doukas, A. D. Zweig, J. K. Frisoli, R. Birngruber, and T. Deutsch, ''Noninvasive determination of shock wave pressure generated by optical breakdown,'' Appl. Phys. B **53**, 237–245 (1991).

[20] G. P. Davidson and D. C. Emmony, ''A schlieren probe method for the measurement of the refractive index profile of a shock wave in a fluid,'' J. Phys. E: Sci. Instrum. **13**, 92–97 (1980).

[21] B. Sullivan and A. C. Tam, ''Profile of laser-produced acoustic pulse in a liquid,'' J. Acoust. Soc. Am. **75**, 437–441 (1984).

[22] M. W. Sigrist, ''Laser generation of acoustic waves in liquids and gases,'' J. Appl. Phys. **60**, R83–R121 (1986).

[23] B. Ward and D. C. Emmony, ''Interferometric studies of the pressures developed in a liquid during infrared-laser-induced cavitation-bubble oscillation,'' Infrared Phys. **32**, 489–515, (1991).

[24] A. P. Alloncle, D. Dufresne, and M. Autric, ''Visualization of laser-induced vapor bubbles and pressure waves,'' in *Bubble Dynamics and Interface Phenomena*, edited by J. R. Blake, J. M. Boulton-Stone, and N. H. Thomas (Kluwer Academic, Dordrecht, The Netherlands, 1994), pp. 365–371.

[25] F. R. Gilmore, ''The growth or collapse of a spherical bubble in a viscous compressible fluid,'' Calif. Inst. Tech. Rep. **26-4** (1952).

[26] R. T. Knapp, J. W. Daily, and F. G. Hammitt, *Cavitation* (McGraw-Hill, New York, 1971), pp. 117–131.

[27] A. Vogel, M. R. C. Capon, M. N. Asiyo-Vogel, and R. Birngruber, ''Intraocular photodisruption with picosecond and nanosecond laser pulses:

tissue effects in cornea, lens, and retina,'' Invest. Ophthalmol. Vis. Sci. **35**, 3032–3044 (1994).

[28] M. S. Habib, M. G. Speaker, R. Kaiser, and T. Juhasz, ''Myopic intrastromal photorefractive keratectomy with the neodymium-yttrium lithium fluoride picosecond laser in the cat cornea,'' Arch. Ophthalmol. **113**, 499–505 (1995).

[29] F. Docchio, C. A. Sacchi, and J. Marshall, ''Experimental investigation of optical breakdown thresholds in ocular media under single pulse irradiation with different pulse durations,'' Lasers Ophthalmol. **1**, 83–93 (1986).

[30] A. Vogel and S. Busch, ''Time-resolved measurements of shock-wave emission and cavitation-bubble generation in intraocular laser surgery with ps and ns pulses,'' in *Bubble Dynamics and Interface Phenomena*, edited by J. R. Blake, J. M. Boulton-Stone, and N. H. Thomas (Kluwer Academic, Dordrecht, The Netherlands, 1994), pp. 105–117.

[31] C. E. Bell and J. A. Landt, ''Laser-induced high-pressure shock waves in water,'' Appl. Phys. Lett. **10**, 46–48 (1967).

[32] M. H. Rice and J. M. Walsh, ''Equation of state of water to 250 kilobars,'' J. Chem. Phys. **26**, 824–830 (1957).

[33] H. Schoeffmann, H. Schmidt-Kloiber, and E. Reichel, ''Time-resolved investigations of laser-induced shock waves in water by use of polyvinylidenefluoride hydrophones,'' J. Appl. Phys. **63**, 46–51 (1987).

[34] W. Lauterborn, ''Kavitation durch Laserlicht,'' Acustica **31**, 51–78 (1974).

[35] Lord Rayleigh, ''On the pressure developed in a liquid during the collapse of a spherical cavity,'' Philos. Mag. **34**, 94–98 (1917).

[36] S. Fujikawa and T. Akamatsu, ''Effects of heat and mass transfer on the impulsive pressure developed by the bubble collapse,'' Bull. JSME **28**, 267–273 (1985).

[37] S. Ridah, ''Shock waves in water,'' J. Appl. Phys. **64**, 152–158 (1988).

[38] F. Docchio, P. Regondi, M. R. C. Capon, and J. Mellerio, ''Study of the temporal and spatial dynamics of plasmas induced in liquids by nanosecond Nd:YAG laser pulses. 1: Analysis of the plasma starting times,'' Appl. Opt. **27**, 3661–3668 (1988).

[39] F. Docchio, P. Regondi, M. R. C. Capon, and J. Mellerio, ''Study of the temporal and spatial dynamics of plasmas induced in liquids by nanosecond Nd:YAG laser pulses. 2: Plasma luminescence and shielding,'' Appl. Opt. **27**, 3669–3674 (1988).

[40] P. K. Kennedy, ''A first-order model for computation of laser-induced breakdown thresholds in ocular and aqueous media: Part I Theory,'' IEEE J. Quantum Electron. **QE-31**, 2241–2249 (1995).

[41] K. J. Ebeling, ''Zum Verhalten kugelförmiger, lasererzeugter Kavitationsblasen in Wasser,'' Acustica **40**, 229–239 (1978).

[42] L. F. Shampine and M. K. Gordon, *Computer Solution of Ordinary Differential Equations. The Initial Value Problem* (Freeman, San Francisco, CA, 1975).

[43] W. Lauterborn and K. Ebeling, ''High-speed holography of laser-induced breakdown in liquids,'' Appl. Phys. Lett. **31**, 663–664 (1977).

[44] J. W. Daiber and H. M. Thomson, ''Laser-driven detonation waves in gases,'' Phys. Fluids **10**, 1162–1169 (1967).

[45] W. M. Flook and D. F. Horning, ''Experimental determination of the thickness of weak shock fronts in liquids,'' J. Chem. Phys. **23**, 816–821 (1955).

[46] W. Eisenmenger, ''Experimentelle Bestimmung der Stoβfrontdicke aus dem akustischen Frequenzspektrum elektromagnetisch erzeugter Stoβwellen in Flüssigkeiten bei einem Stoβdruckbereich von 10 atm bis 100 atm,'' Acustica **14**, 187–204 (1964).

[47] P. Harris and H. N. Presles, ''The shock induced electrical polarization of water,'' J. Chem. Phys. **74**, 6864–6866 (1981).

[48] P. Harris and H. N. Presles, ''Reflectivity of a 5.8 kbar shock front in water,'' J. Chem. Phys. **77**, 5157–5164 (1982).

[49] L. D. Landau and E. M. Lifschitz, *Hydrodynamik* (Akademie Verlag, Berlin, 1991).

[50] O. V. Rudenko and S. I. Soluyan, *Theoretical Foundations of Nonlinear Acoustics* (Consultants Bureau, Plenum, New York, 1977).

[51] J. M. Richardson, A. B. Arons, and R. R. Halverson, ''Hydrodynamic properties of sea water at the front of a shock wave,'' J. Chem. Phys. **15**, 785–795 (1947).

[52] M. Müller, ''Stoβwellenfokussierung in Wasser,'' Ph.D. thesis, Rheinisch-Westfälisch Technische Hochschule Aachen, Aachen 1987.

[53] J. Noack and A. Vogel, ''Streak photographic investigation of shock-wave emission after laser-induced plasma formation in water,'' Proc. SPIE **2391**A, 284–293 (1995).

[54] T. A. Dunina, S. V. Egerev, L. M. Lyamshev, K. A. Naugol'nykh, and A. E. Pashin, ''Hydrodynamic effects in the optical breakdown of a liquid,'' Sov. Phys. Acoust. **28**, 116–121 (1982).

[55] V. S. Teslenko, ''Investigation of photoacoustic and photohydrodynamic parameters of laser breakdown in liquids,'' Sov. J. Quantum Electron. **7**, 981–984 (1977).

[56] A. P. Alloncle, J. Vierne, M. Autric, and D. Dufresne, ''Laser-induced dielectric breakdown in a transparent liquid,'' Proc. SPIE **2273**, 98–107 (1994).

[57] A. B. Arons, ''Underwater explosion shock wave parameters at large distances from the charge,'' J. Acoust. Soc. Am. **26**, 343–346 (1954).

[58] P. H. Rogers, ''Weak-shock solution for underwater explosive shock waves,'' J. Acoust. Soc. Am. **62**, 1412–1419 (1977).

[59] V. A. Akulichev, Yu. Ya. Boguslavskii, A. I. Ioffe, and K. A. Naugol'nykh, ''Radiation of finite amplitude spherical waves,'' Sov. Phys. Acoust. **13**, 281–285 (1968).

[60] R. Hickling and M. S. Plesset, ''Collapse and rebound of a spherical bubble in water,'' Phys. Fluids **7**, 7–14 (1964).

[61] S. Fujikawa and T. Akamatsu, ''Effects of the non-equilibrium condensation of vapour on the pressure wave produced by the collapse of a bubble in a liquid,'' J. Fluid Mech. **97**, 481–512 (1980).

[62] L. B. Poché, ''Underwater shock-wave pressures from small detonators,'' J. Acoust. Soc. Am. **51**, 1733–1737 (1971).

[63] Y. V. Petukhov, ''Modified Kirkwood-Bethe approximation suitable for calculating the complete profile of a detonation wave and its spectrum near the source,'' Sov. Phys. Acoust. **33**, 185–188 (1987).

[64] A. G. Doukas, D. J. Mc Aucliff, and T. J. Flotte, ''Biological effects of laser-induced shock waves: Structural and functional cell damage in vitro,'' Ultrasound Med. Biol. **19**, 137–146 (1993).

[65] A. Vogel, R. Engelhardt, U. Behnle, and U. Parlitz, ''Minimization of cavitation effects in pulsed laser ablation—illustrated on laser angioplasty,'' Appl. Phys. B **62**, 173–182 (1996).